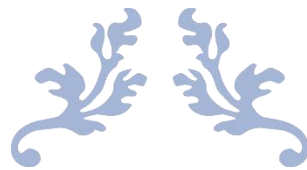




University of
Nottingham

UK | CHINA | MALAYSIA



THE DEVELOPMENT OF CATALYSTS
AND ADSORBENTS FOR
ENHANCED ELEMENTAL MERCURY
REMOVAL AT ESPS AND FGDS AT
COAL-FIRED POWER STATIONS

Liwen Zhang, BEng



DISSERTATION SUBMITTED TO THE UNIVERSITY OF
NOTTINGHAM FOR THE DEGREE OF MASTER OF RESEARCH

Acknowledgement

I would like to express my sincere appreciations and gratitude to Professor Tao Wu and Dr. Haitao Zhao for their invaluable guidance and support throughout the period of my MRes period. Working with them provided an enriching experience to my academic life at the University of Nottingham, Ningbo, China. Their encouragement and support were instrumental in the completion of my thesis.

Research Council [grant numbers EP/G037345/1 and EP/L016362/1]. National Key R&D Program of China (2017YFB0603202) is acknowledged for partially sponsored this research. Most important of all, I would like to thank my parents and my entire family for their encouragement and support, both for PG study and my whole life.

I would like also to express my thanks to the staff members who helped and gave me precious suggestions in research work and experiments, especially Dr. Mengxia Xu, Gang Yang, Dr. Xiang Luo, Dr. Yipei Chen, Carey Tao, Kelly Yao, Helen Xu etc. I also appreciate the help and support from all my colleagues and friends: Dr. Yuxin Yan, Shuai Liu, Peng Jiang, Jiahui Yu, Fengjuan Song, Dr. Shu Liu, Dr. Huayang Li, Jinwei Cao, etc.

Contents

Chapter 1 Introduction.....	5
Chapter 2 Literature review.....	8
2.1 Introduction.....	8
2.2 Mercury toxicity.....	9
2.3 Mercury Source.....	10
2.4 Research status of mercury removal technology in coal-fired flue plant.....	11
2.4.1 Pre-combustion mercury removal technology.....	12
2.4.2 Technologies of mercury removal in combustion.....	12
2.4.3 Post-combustion mercury removal technologies.....	13
2.5 Summary.....	18
Chapter 3 Experimental.....	20
3.1 Research method.....	21
3.2 Chemicals and reagents.....	23
3.3 Experimental instruments.....	24
3.4 Preparation of catalysts.....	25
3.5 Hg ⁰ removal experiments.....	25
Chapter 4 Performance of Mn/Mo-Mn catalytic in Hg⁰ removal.....	27
4.1 Hg ⁰ removal efficiency analysis.....	27
4.1.1 Hg adsorption and catalytic oxidation performance evaluation.....	27
4.1.2 Quantitative analysis for evaluating Hg ⁰ catalytic oxidation.....	29
4.2 Characterizations.....	32
4.2.1 XRD.....	32
4.2.2 BET.....	34
4.2.3 TEM.....	35
4.2.4 DRIFT.....	37

4.3 Summary.....	38
Chapter 5 Performance of Cu-S/Cu-Mo-S adsorbent in Hg⁰ removal.....	40
5.1 Hg ⁰ removal efficiency analysis.....	40
5.1.1 Dynamic transient screening of adsorbents.....	40
5.1.2 Steady state evaluation.....	42
5.1.3 Space velocity analysis.....	44
5.2 Characterizations.....	46
5.2.1 XRD.....	46
5.2.2 XPS.....	47
5.2.3 BET.....	48
5.2.4 TEM.....	49
5.3 Summary.....	51
Chapter 6 Conclusions.....	52
References.....	54

Chapter 1 Introduction

Mercury is a highly toxic pollutant produced by coal combustion.[1] The emission of mercury fume causes a severe impact on the ecosystem and human health, attribute to its high volatility and persistent exist properties. Furthermore, mercury can be accumulated through the biological chain and cause further threats to the environment. The gaseous elemental mercury is the main form of mercury pollution around the world and it is emitted into the atmosphere due to industrial activities (power plants). Based on the findings of studies, mercury emission from the coal-fired power plant has made up to approximately 13.2% (292tonnes) in 2015 and the anthropogenic activities are considered as the main factors for that consequences[2]. Therefore, regulations have already been made both locally and globally on controlling atmospheric emission. To date, an international treaty called Minamata Convention has been ratified by 123 countries. Under the Minamata Convention, from 2017, States parties already prohibited the manufacturing, importing, and exporting mercury-containing coal. Furthermore, novel mercury control technology, especially for mercury emissions in coal-fired flue gas, is currently the main technical requirement.

Mercury released from coal-fired power plant exists in three forms: elemental mercury (Hg^0), oxidized mercury (Hg^{2+}) and particulate bound mercury (Hg^p)[3]. At typical air emissions and operating temperatures Hg^0 has a high vapour pressure, which also increases the removal complexity. Mercury oxide, unlike Hg^0 , because it is easy to contact particulate matter is easily removed in Wet flue gas desulfurization unit (WFGD) equipment and easily collected by Electrostatic Precipitators (ESP) and Fabric Filter(FF)[4]. Hg^0 is the hardest to remove because of its high volatility and low solubility. Currently, adsorbent injection for boiler optimization and SCR (original activated carbon or reformed activated carbon), halogen salt (e.g. CaBr_2) is a commercially available mercury release control technology. Since the nature of coal and the equipment of power plants are very different, there is no general mercury control plan that can be applied in all cases, and it is always necessary to combine

control methods. Activated carbon injection is the deepest and most mature method, but at a high price. The United States department of energy estimates that removing a pound of mercury will cost between \$25,000 and \$70,000 to 90 per cent if absorbed[5]. In addition, in high-sulphur coal conditions, the emission potential of activated carbon was clearly reduced. Therefore, removal of Hg^0 flue gas from coal-fired process flue gas or convert Hg^0 to Hg^{2+} , which is easy to remove, is crucial to mercury emission control.

One method that can be considered is to use the oxidation of precious metals or transition metal for catalytic oxidation reaction with Hg^0 and produce Hg^{2+} . Then the WFGD system can easily remove it. However, although precious metals such as gold (Au) and palladium (Pd) have been proved to have good catalytic oxidation properties, their application cost in industries is too expensive[6]. Additionally, in practical applications, the presence of sulfur dioxide (SO_2), a common component in coal flue gas can inhibit the catalytic oxidation of Hg^0 . Therefore, much work so far has focused on the method of SCR and Hg^0 cooperative, which can convert the SO_2 through a catalyst into SO_3 . Furthermore, the conversion efficiency can be improved by using dopants. Among all dopants, Mo is the dopant with the best effect of removing SO_2 interference[7].

Considering economic efficiency, using transition metal oxides to remove mercury is an effective approach such as copper oxide (CuO_x), cobalt oxide (CoO_x), and manganese oxide (MnO_x) were selected for Hg^0 removal. At present, MnMo catalyst and Cu base adsorbent have been selected as the better combination for Hg^0 removal. There were study on the optimization of Mo doping ratio[8].

In this study, a series of MnMo/ γ - Al_2O_3 catalysts and CuMoS/ γ - Al_2O_3 adsorbent with different ratios were synthesized by initial wet impregnation (IWI) method, and the removal performance of Hg^0 was studied. In previous work, the optimization of Mo doping ratio has been completed[9]. Therefore, the main purpose of this study is to optimize the MnMo/ γ - Al_2O_3 catalysts and CuMoS/ γ - Al_2O_3 adsorbents according to the performance test of mercury removal energy. The effect of Mo addition on

catalysts and adsorbents were elucidated through system characterization, and the optimal proportion of active ingredients was optimized.

(1) Catalysts preparation.

Using γ -Al₂O₃ as the carrier, MnOx/ γ -Al₂O₃ and MnOx-MoO₃/ γ -Al₂O₃ catalyst and Cu-S/ γ -Al₂O₃ and Cu-Mo-S/ γ -Al₂O₃ adsorbents with different manganese content are prepared via incipient-wetness impregnation method in this project.

(2) Demercuration performance study.

The demercuration performance is studied by qualitative and quantitative analysis, while the demercuration performance of catalysts is measured via temperature programmed surface reaction (TPSR). The catalyst's performance in terms of adsorption and catalytic oxidation of Hg⁰ are tested under 30 °C ~700 °C dynamic temperature programmed experiment condition. The removal effect of Hg⁰ is probed via qualitative analysis, while the catalytic oxidation effect of Hg⁰ is studied via quantitative analysis.

(3) Structural characterization.

The relationship between the structure, morphology and catalytic performance of catalysts is probed via systematic characterization. XRD and TEM characterization are used to study the relationship between crystal plane and lattice and oxygen vacancy on catalyst surface, as well as the influences on catalytic oxidation. BET is used to characterize the influences of specific surface area on adsorption effects. The relationship between acidity sites on catalyst surface and demercuration performance is studied via in-situ FTIR characterization. The influences of pre-doping of molybdenum on manganese-based catalyst, as well as the synergistic effects between molybdenum and manganese after the addition of molybdenum, are thereby proved via mechanism analysis.

Chapter 2 Literature review

2.1 Introduction

Mercury and its compounds are toxic and harmful substances. Small doses of mercury can cause great harm to human health, the ecological environment, soil, water, and air[10]. Moreover, mercury has the characteristics of strong latent toxicity transfer in food chain enrichment in migrating organisms from region to region[11]. Mercury entering the atmospheric environment is ultimately a global pollutant undergoing atmospheric circulation. Oxidised mercury can settle near the emission source only after staying in the atmosphere for a few days, while elemental mercury can remain in the atmosphere for several years, thus being transmitted and distributed over a long distance, which is the main source of mercury migration and pollution on a global scale[12]. Mercury entering the aquatic environment mainly reacts with sulphate on the surface of sediments to form insoluble mercury sulphide. Mercury in the bottom mud of aquatic environments can be transformed into methylmercury under the action of microorganisms. Methylmercury redissolves in water and concentrates in aquatic organisms, making it one of the most toxic mercury compounds[13]. Mercury entering soil and water bodies due to sedimentation is released back into the atmosphere to participate in the migration of atmospheric mercury, and settles again in the form of gaseous or particle attachment, forming secondary emissions and pollution[14]. In general, background concentrations of mercury in the atmosphere do not constitute a hazard to human health; therefore, mercury pollution is fundamentally caused by mercury emissions from the development and use of mercury. In addition to natural causes (e.g. volcanic eruptions, rock weathering, and forest fires), human activities (e.g. the production of chlor-alkali from the burning of fossil fuels, metal smelting, and cement) have become important sources of atmospheric mercury pollution[15].

Coal, as a type of non-clean energy, is the main cause of air pollution. Coal for power generation is the main reason for the increase in coal consumption. Burning coal for power generation leads to the emission of gaseous pollutants such as NO_x, SO₂, and

Hg⁰ to the atmosphere. If these gaseous pollutants are not controlled, serious environmental problems will occur, such as acid rain haze, photochemical smog, and Minamata disease. A lot of research has been undertaken on coal in China, and results have shown that mercury levels vary widely depending on the location and type of coal. For example, the average mercury concentration in Chinese coal is 0.22 ppm, but in some samples from Guizhou it has been found to reach 7.2 ppm, 10.5 ppm, or even 55 ppm[16]. Despite the relatively low mercury concentrations in coal, huge amounts of mercury are released into the atmosphere each year from coal burning worldwide. Mercury is a highly toxic element that is released through natural and anthropogenic emissions, and poses a serious threat to human health and ecosystems owing to its unique characteristics of bioaccumulative volatility and durability. Due to the potential harm of mercury to biological systems, especially to human health, mercury emissions have attracted increasing attention. Among the various emission sources, coal-fired power plants are the largest known source of anthropogenic mercury. Therefore, reducing mercury emissions from coal-fired power plants is a global goal. At present, China attaches great importance to NO_x and SO₂ pollution control, and the technology has matured[17]. On the contrary, there is a lack of emphasis on Hg pollution control, and emission standards are far lower than those in developed countries. Therefore, the development of an economical and efficient technology for mercury removal from coal flue gas in China is urgently needed[16].

2.2 Mercury toxicity

Mercury is one of the major lethal pollutants, while metallic mercury vapour, organic mercury, and inorganic mercury are all highly toxic. Mercury and its compounds are mainly absorbed by the human body in three ways: via the skin, respiratory tract, and digestive tract[18]. Over 95% of organic mercury compounds can be absorbed by the digestive tract, and mainly harm the central nervous system, kidney, and digestive system of the human body, but can also harm the skin, respiratory system, blood, and eyes[19]. After entering the human body, mercury from mercury compounds may combine rapidly with tissue protein and the sulfhydryl group of blood to provide a

certain mercury detoxification capacity in the human body. Mercury then gradually accumulates in the kidneys, which are the functional organ for detoxification of the human body, thus causing kidney failure. Once inorganic mercury enters a waterbody through air deposition, it can be transformed into the most toxic methylmercury by biomethylation under anaerobic conditions. It can subsequently enter the human body via the food chain, causing nervous system disorder, liver and kidney injury, and child development damage. Mercury poisoning includes acute and chronic mercurialism; the former is mainly caused following the absorption of high-concentration mercury vapour over a short period of time, while the latter is mostly occupational disease, with symptoms of headaches, tremors, and testiness, and may cause mental disorders and kidney failure in severe cases[20].

The Japanese “minamata disease” incident occurred in the 1950s and affected more than 10 000 residents after eating methylmercury-containing fish over a long period of time[3]. Such incidents also occurred in the mid-1960s, when mercury poisoning cases appeared due to the continuous discharge of mercury- and methylmercury-containing wastewater from a chemical plant in the Songhua River basin. The harmfulness of mercury pollution has gained attention worldwide, especially the mercury pollution associated with coal-fired power plants. The United States and the European Union issued the Mercury Emission Standard of coal-fired power plants in 2011 and 2005, respectively. In 2013, driven by the United Nations Environment Programme (UNEP), representatives from 186 countries and regions around the world signed the International Mercury Convention: *Minamata Convention*. China’s latest *Air Pollutant Release Standard for Heat-Engine Plant* (GB13223- 2011) stipulates that the discharge concentration of mercury and its compounds shall not exceed 0.03 mg/m³. With increasingly strict mercury emission standards, technology to control mercury pollution in coal-fired power plants is urgently needed[21].

2.3 Mercury Source

There are two main sources of mercury pollution in the atmosphere: natural sources, including mercury discharged by rock weathering, volcanic eruptions, ocean

movement, forest fires, and other natural phenomena; and anthropogenic sources, such as mercury extraction and purification from ore smelting, fossil fuel combustion, chlor-alkali and electrical equipment industry, and coal burning, which is the main source of atmospheric mercury pollution[22]. As the largest anthropogenic mercury emission source in the world, coal-fired power plants contribute approximately one-third of the mercury emission source.

According to the UN's 2013 pollution report, global mercury emissions in 2010 were 2600 t, 75% (1960 t) of which were man-made. The amount of mercury released in 2010 was only 40% of the current level of mercury in the atmosphere. The remaining 60% of atmospheric mercury is associated with earlier releases. According to these reports, China's mercury emissions are much higher than those of other countries. In 2005, China emitted approximately 830 t of mercury, almost as much as the next few high-emitting countries combined[23]. However, the main source of mercury emissions in China is coal, which emits approximately 400 t, most of which is for power generation and industrial use. Effective control of mercury emissions from coal burning can effectively reduce the total amount of mercury emissions in China[24].

2.4 Research status of mercury removal technology in coal-fired plant

Mercury in the flue gas of coal-fired power plants has three forms: elemental mercury (Hg^0), mercuric oxide (Hg^{2+}), and particulate mercury (Hg^{P})[25]. Both Hg^{2+} and Hg^{P} are easily adsorbed by coal ash and removed by the existing coal-fired flue gas pollutant control equipment, while Hg^{2+} is soluble in water and can be removed using wet desulphurisation devices. However, Hg^0 is difficult to remove from existing power plant equipment because of its strong chemical stability and insolubility in water[26]. Therefore, the difficulty of coal-fired flue gas demercuration is Hg^0 adsorption and catalytic oxidation. According to the research status both in China and abroad, the demercuration process of coal-fired power plants currently mainly includes pre-combustion mercury removal, mercury removal in the combustion process, and post-combustion mercury removal.

2.4.1 Pre-combustion mercury removal technology

Pre-combustion mercury removal mainly refers to coal washing and heat treatment technologies. As a trace element, mercury mainly exists in the iron pyrite of coal in the inorganic compound state. Therefore, an organic flotation agent can be added to the coal washing stage to realise mercury sediment removal. Research has shown that the mercury removal rate of coal washing technology can reach 21%–37%. Although it has the advantages of low cost and being a relatively proven technique, coal washing technology can only remove a small amount of mercury. In addition, the washing rate of China's raw coal is only 22%, which is far below the standards of developed countries[27]. Therefore, it is difficult to reduce China's mercury emissions from coal burning by relying solely on coal washing technology. The volatile characteristics of mercury and its compounds are utilized in the heat treatment technology of raw coal at high temperatures and high pressures, thus volatilising mercury and its compounds. In addition, the mixed combustion of coal and biomass fuel can increase the chlorine content of the combustion process and improve the mercury removal efficiency. However, partial decomposition also occurs during the heating process of coal, leading to a lower calorific value. Therefore, coal washing technology is relatively more advanced, and the heat treatment technology of coal is not applicable for large-scale industrial applications.

2.4.2 Technologies of mercury removal in combustion

According to the research status both in China and abroad, there are fewer studies on mercury removal technology during the combustion process compared with pre-combustion technologies. Mercury removal during the combustion process mainly includes changing the combustion conditions and adding additives to coal, which transform mercury into an easy-to-remove form, and remove it through the flue gas treatment device[26]. Temperature, atmosphere, and pulverised coal fineness all affect the combustion process, and the specific technologies include fluidised bed combustion, low-carbon combustion, and low-nitrogen combustion technologies. In the fluidised bed combustion method, the standing time of flue gas in the furnace is

increased to improve the oxidation rate of mercury and the adsorption opportunity of particles produced in the combustion process. The additives added to the treated coal mainly include limestone, potassium iodide, and calcium bromide, which can change the form of mercury and improve the mercury removal efficiency. However, they also produce new pollutants and corrode equipment.

2.4.3 Post-combustion mercury removal technologies

Post-combustion mercury removal refers to mercury removal from flue gas, which is the key to mercury removal technology, and with the constantly improving environmental standards of various countries, mercury removal from flue gas may become the key to mercury pollution control technology of coal-fired power plants. Currently, flue gas dust removal, desulphurisation, and denitrification equipment in coal-fired power plants are mature; therefore, improving the mercury removal efficiency of flue gas based on existing equipment and devices will become a future research focus. Many studies have been conducted on post-combustion mercury removal technology, mainly including adsorption methods, normal pollutant control devices, catalytic oxidation methods, photocatalysis, and plasma technology[28].

2.4.3.1 Removal of mercury by adsorption

The commonly used adsorbents for mercury removal in adsorption method include activated carbon, fly ash, calcium based adsorbent mineral material adsorbent and metal oxide adsorbent, etc. Adsorbents with highly developed pore structure not only have strong physical adsorption capacity to mercury, but also are good carriers for various active components. Adsorbents with highly developed pore structure not only have strong physical adsorption capacity to mercury, but also are good carriers for various active components.

(1) Activated carbon adsorbent

Activated carbon has developed pore structure and higher specific surface area. It is an efficient adsorbent for mercury removal. The adsorption of mercury on activated

carbon includes the physical process and chemical reaction, such as adsorption, condensation and diffusion. The mercury removal efficiency is mainly related to the physical properties of the adsorbent itself (particle size, aperture, surface area, etc.), temperature and residence time of flue gas components, mercury concentration and other factors. Mercury removal from activated carbon can be divided into two types according to adsorption mechanism: The first mechanism relies on the special pore structure and a large number of micro-pores on the surface of the adsorbent to remove mercury through strong physical adsorption capacity. Another type of mechanism depends on the abundant organic functional groups (such as carboxyl, hydroxyl, carbonyl, lactone, etc.)[29] on the surface of the adsorbent, which have good chemisorption ability. Activated carbon adsorbent for mercury removal is the most mature and popular technology for mercury removal from flue gas in coal-fired power plants, and it is widely used in the world. In order to further improve the mercury adsorption performance of activated carbon, many researchers modified activated carbon with halogens and so on. The mercury removal ability of modified activated carbon is improved, but the cost is increased due to the decrease of activated carbon utilization. Moreover, the poor thermodynamic stability also limits the use of activated carbon adsorbent in the face of complex flue gas, resulting in the limitations of activated carbon in the removal of mercury from flue gas[30].

(2) Fly ash and calcium-based adsorbents

Fly ash refers to the coal ash produced after combustion, which has the advantages of small particle size, practicality, high cost and so on. The source of fly ash is the product of fuel combustion, so it can be obtained by combining with the existing fly ash removal technology. Compared with activated carbon adsorbent, fly ash is a kind of adsorbent with lower cost. The adsorption of mercury by fly ash includes physical adsorption, chemical adsorption and chemical reaction. The adsorption performance of mercury is mainly attributed to the unburned carbon in fly ash. In addition, MnO, MgO, Fe₂O₃ and oxygen-containing functional groups on the surface also have catalytic oxidation effect on mercury[31]. The smaller the particle size of fly ash is,

the stronger the mercury removal ability is, and the better the mercury removal adsorbent can be obtained by modifying it.

(3) Mineral adsorbents

Mineral adsorbents are mainly made of minerals with abundant reserves, low price and no toxicity to the environment. Its composition is mainly some clay minerals, including zeolite, vermiculite, kaolin, diatomite, bentonite, etc.. For example, the synthetic zeolite is generally called molecular sieves, is the use of alumina clay silica and alkali as raw materials synthesis, often used as gas and liquid desiccant adsorbent and carrier[32]. In structure, it has many holes with uniform pore size and well-arranged pores. Molecular sieves with different pore sizes separate molecules of different sizes and shapes. The adsorption capacity of these mineral materials is not high, and the mercury adsorption capacity can be greatly improved by modifying them. The preparation of low cost and high efficiency mercury removal adsorbents by mineral modification has been a research hotspot in recent years[33].

(4) Metal oxide adsorbents

Metal oxide adsorbent is a potential adsorbent for mercury removal, especially the transition metal, showing good oxidation performance[34]. Because lattice oxygen in metal oxides has a strong oxidation property, it has a good effect on the oxidation of elemental mercury. Metal oxides include single metal oxides and bimetal oxides and various metal oxide complexes. Some of the metal oxides (such as Al_2O_3 and SiO_2)[35] have good mechanical properties, high specific surface area and well-developed pore structure, making them ideal carriers for adsorbents.

2.4.3.2 Removal of mercury by catalytic oxidation

Removal of Hg^0 from flue gas is key to mercury removal technology. Compared with other methods, catalytic oxidation technology is one of the most promising technologies for mercury removal. This technology can be reused many times and can maintain a long-term high efficiency without secondary pollution. Catalytic oxidation

refers to the oxidation of elemental mercury (Hg^0) in flue gas to oxidised mercury (Hg^{2+}) through the synergistic action of the catalyst and oxidising substances in the flue gas. Mercury ions are highly water-soluble, easily adsorbed, and can be removed by other flue gas treatment equipment. At present, most studies on catalytic oxidation methods use HCl or Cl_2 in flue gas as oxidants, but the concentrations of these two oxidants in flue gas is relatively low[21]. On the contrary, O_2 , as the most commonly used oxidant, also has a high concentration in coal-fired flue gas. The use of O_2 as an oxidant to achieve the oxidation of mercury in the absence of HCl is the current research focus of catalytic oxidation technology[36]. On the contrary, O_2 , as the most commonly used oxidant, also has a high concentration in coal-fired flue gas. The use of O_2 as an oxidant to achieve the oxidation of mercury in the absence of HCl is the current research focus of catalytic oxidation technology[16].

Owing to the complex composition of flue gas and the long operation time of mercury removal equipment, the catalyst requirements are high. Mercury removal catalysts resist poisoning and maintain catalytic activity under a wide temperature window with low cost and long service life. Currently, selective catalytic reduction (SCR) catalysts[37] and metal and metal oxide catalysts are most commonly used, and are mainly divided into two categories: supported catalysts and non-supported catalysts. A supported catalyst consists of at least two components: a carrier and an active component. Common carriers include $\gamma\text{-Al}_2\text{O}_3$, activated carbon, and molecular sieves, which are characterised by large specific surface areas and more micropores and reaction sites than other carriers[38]. The active components include precious metals and transition metals. Transition metal oxides have become a research hotspot in recent years because of their low cost and low activity, and mainly include V, Co, Cr, Ce, Mo, and Mn[39]. The main synthesis methods for non-supported catalysts include sol-gel and co-precipitation methods. These methods utilise the interaction between different components to form a porous structure and increase the specific surface area of the catalyst. However, the synthesis process is uncontrollable, with complex interactions among various components and many influencing factors. Therefore, the

pore structure of the synthesis catalyst is disordered and the pore diameter distribution is not concentrated, which seriously affects the effect of mercury removal[40].

(1) Molybdenum-based catalysts

Molybdenum-based catalysts have been widely studied in recent years because of their excellent catalytic performance and low price. Molybdenum is a transition metal with variable valence. There are a variety of molybdenum-based catalysts, mainly oxide sulphide nitrides. Molybdenum disulphide, a two-dimensional transition metal with a graphene-like structure, is widely used in catalytic studies[13]. Molybdenum-based catalysts are mainly used in the production of acrylonitrile methane dry-reforming by hydrodesulphurisation propane ammoxidation of petroleum. In addition, MoO_3 has been widely used as a stabiliser and promoter to improve the active mechanical properties and structural properties of NH_3 -SCR reaction catalysts owing to its excellent anti-sulphur toxicity properties. The synthesis methods of molybdenum-based catalysts mainly include the impregnation chemical vapour-deposition solvent thermal ion-exchange method[41].

(2) Manganese-based catalysts

Manganese oxides have the strongest catalytic abilities among existing metal oxides in nature[40], and manganese-based catalysts are considered to be among the most promising catalysts for mercury removal because of their high catalytic oxidation performance, low cost, and environmental friendliness. Manganese oxides mainly include MnO , MnO_2 , Mn_2O_3 , and Mn_3O_4 , among which MnO_2 has the most outstanding performance because Mn^{4+} has a stronger oxidation capacity than other species of Mn[42]. These manganese oxides have excellent physical and chemical properties, such as high reversible capacitance structures, flexible stabilities, high charge and discharge rates, and fast cation diffusion rates. Manganese oxides have wide application prospects and can be used as adsorbent catalysts for electrode materials. In addition, manganese-based materials usually have high structural flexibility and can be modified by catalyst carriers and other elements[17]. The

application of manganese oxides in a gas polyphase catalytic reaction was proposed several decades ago, and the material exhibited a strong polyphase catalytic performance. At present, manganese-based oxides are commonly used for the SCR of NH_3 , catalytic combustion, Hg^0 adsorption, and the catalytic oxidation of CO.

2.4.3.3 Novel demercuration technologies

Photocatalysis is defined as the direct and indirect oxidation and reduction reactions on the surface of materials caused by photogenerated holes and electrons generated via the activation of semiconductors by light sources. In recent years, owing to its affordable price, high chemical stability, strong oxidation, and lack of secondary pollution, public attention has been focused on photocatalytic technology. Photocatalytic oxidation demercuration uses highly reactive oxygen produced by a catalyst under a light source to react with mercury in flue gas to oxidise mercury to Hg^{2+} , which is then captured by a part of the subsequent device. Currently, the commonly used photocatalysts include TiO_2 , C_3N_4 , and BiVO_4 [43]. This method is still at the experimental stage and needs further investigation before it can be used in an actual device for demercuration[44].

Plasma technology has also been used for demercuration in recent years. There are various ways to generate plasma, and currently, corona discharge is the most profusely explored method in flue gas treatment[45]. Dielectric barrier discharge plasma technology blocks discharge via dielectrics and converts simple mercury in flue gas into divalent mercury. However, few application examples exist owing to the immaturity of this technology; hence, further study is required. The uniquely elusive property of mercury limits the application of plasma technology in demercuration[34].

2.5 Summary

To date, many studies have investigated mercury. The first and most basic was Kevin et al.[46], who reviewed the migration and transformation law of mercury during coal combustion. The authors laid the theoretical foundation for removing mercury from coal-fired power plants. Mineral adsorbents have been a popular research topic of

mercury removal in recent years. Mineral adsorbents used for mercury removal are characterised by their abundant reserves and low cost. The mineral adsorbent commonly used is ash (including fly ash) pyrite. Modification and improvement are generally required to improve the mercury removal efficiency of mineral adsorbents. Xu et al.[47] conducted X-ray fluorescence and X-ray electron spectroscopy tests, and found that mercury removal from fly ash was mainly due to its physical and chemical adsorption. Fly ash has a high specific surface area and small pore size, which are conducive to improving the efficiency of mercury removal. However, the conditions for the use of mineral adsorbents in power plants are still harsh. High temperatures will enable the catalytic oxidation ability of some active components, which is not conducive to the adsorption of Hg^0 .

Technologies for mercury removal by metal catalysts focus on the oxidation capacity and high specific surface area of metal catalysts, and modification is sometimes needed to improve the efficiency of mercury removal by metal catalysts. At present, many types of metal catalysts have been investigated. Kokkinos et al.[48] chose tetravalent manganese ferrihydrite as a catalyst based on its high oxidation capacity, high surface area, and high negative charge density. Yi Zhao et al.[49] synthesised a CoFe_2O_4 catalyst using the sol-gel method, finding that Co and Fe could oxidise Hg^0 to Hg^{2+} through a series of reactions, and that the efficiency of mercury removal reached 85%. Ma et al.[50] designed a layered mixed-oxide structure of $\text{MnO}_2/\text{CeO}_2\text{-MnO}_2$. The results showed that the synthesised catalyst had rich surface oxygen and a layered pore structure, and the removal efficiency of Hg^0 reached 89% because the pore structure was conducive to the adsorption of gaseous mercury. The basic active site for Hg^0 oxidation is MnO_2 , while CeO_2 promotes the synthesis of O_2 and improves the oxidation characteristics of MnO_2 . Liu et al.[51] analysed the unsaturated metal potential based on density functional theory (DFT) and concluded that Hg^0 could stabilise the unsaturated metal potential existing in the organic framework of metals. This also provided a strong condition for the further oxidation of Hg^0 . These catalysts can be re-oxidised under oxygen, which can facilitate their

reuse. To further reduce the cost of mercury removal, some scholars have investigated the use of renewable mercury removal technology[52]. In the future, mercury removal technology should be developed to improve the efficiency of mercury removal and reduce the application cost of mercury removal technology by combining multi-pollutant emission control.

Chapter 3 Experiments

3.1 Research method

In this study, a catalyst for mercury removal from coal-fired flue gas was developed via the incipient-wetness impregnation method, which features low cost, high catalytic oxidation performance and environmental friendliness. The demercuration performance was studied via temperature-programmed surface reaction (TPSR), and the optimal temperature for demercuration was determined by steady-state analysis. On top of that, the demercuration mechanism based on Mn catalyst modified from Mo was optimized by a series of systematic characterization.

The specific surface area (S_{BET}) of the catalysts was measured through Micromeritics ASAP 2020 to give the information of pore volume and average pore size. The pore size and distribution of the catalyst restricted the internal diffusion resistance of the reactants and products and the relative concentration of the surface reactants, so the specific surface area was an essential parameter for the surface and morphology of the reaction catalyst. X-ray Diffraction XRD (Bruker, Germany) was a method conducted to find the pattern diffracted by X-ray and analyze the crystallinity of the catalysts. To explore the influence of dopants on the catalyst, we used *in-situ* diffuse reflectance infrared Fourier transform spectroscopy (*in-situ* DRIFTS) as an effective means to study the surface reaction mechanism of catalysts. In this study, the acid sites of the catalysts were explored. (Using NH_3 as the alkaline probe molecule, we can treat Hg as an alkaline gas). According to the *in-situ* DRIFTS experiments, the temperature-programmed desorption (TPD) was used to study adsorption and desorption behaviour of NH_3 (Simulation of mercury) on the samples' surface. The adsorption capacity of catalyst to Hg was explained by analyzing the peak strength. Transmission electron microscope (TEM) and high-resolution transmission electron microscopy (HRTEM) images were captured via a JEM 2100 microscope operated at 200 kV. TEM can clearly observe the metal-supported catalyst, and analyze the arrangement of the constituent atoms and the direction of crystal growth.

The relationship between the structure, morphology and catalytic performance of catalysts was probed via systematic characterization. XRD and TEM characterization were used to study the relationship between crystal plane, lattice and oxygen vacancy on the catalyst surface, as well as the influence on catalytic oxidation. BET was used to characterize the influence of specific surface area on adsorption effects. The relationship between acidity sites on the catalyst surface and demercuration performance was studied via in-situ FTIR characterization. The influence of pre-doping of molybdenum on the manganese-based catalyst, as well as the synergistic effects between molybdenum and manganese after the addition of molybdenum, were thereby proved via mechanism analysis.

3.2 Chemicals and reagents

The reagents and chemicals applied in this chapter are listed in Table 1.1.

Table 1.1. Main chemicals and reagents used in the experiments

Chemicals	Molecular formula	Standard	Supplier
Ammonium molybdate	$(\text{NH}_4)_6\text{Mo}_7\text{O}_{24}\cdot 4\text{H}_2\text{O}$	AR	Sinopharm Chemical Reagent Co., Ltd.
Manganese nitrate (Tetrahydrate)	$\text{Mn}(\text{NO}_3)_2\cdot 4\text{H}_2\text{O}$	AR	Sinopharm Chemical Reagent Co., Ltd.
Cupric Nitrate (Hexahydrate)	$\text{Cu}(\text{NO}_3)_2\cdot 6\text{H}_2\text{O}$	AR	Sinopharm Chemical Reagent Co., Ltd.
Aluminium oxide (Gamma)	$\gamma\text{-Al}_2\text{O}_3$	Size range: $1.18 \leq X \leq 1.70\text{nm}$	V-SK Co., Ltd.
Nitrogen	N_2	99.999%	Dalian Anruisen Special Gas Co. Ltd.
Argon gas	Ar	99.999%	Dalian Anruisen Special Gas Co. Ltd.
Hydrogen sulfide	H_2S	99.999%	Dalian Anruisen Special Gas Co. Ltd.

3.3 Experimental instruments

The instruments and equipment applied in this chapter are listed in Table 1.2.

Table 1.2. Instruments and equipment

Instrument	Model	Supplier
On-line mercury analyzer	Tekran 3300RS	Tekran Instruments Co. Ltd
Tubular furnace (vertical)	60250-12-6A	Hangzhou Zhuoke Instrument Co. Ltd.
Tubular furnace (horizontal type)	GSL1700X	Zhengzhou Kejing electric Furnace Co. Ltd.
Air drying oven	DHG-9070A	Shanghai Yiheng Scientific Instrument Co., Ltd.
Electronic balance	FA2104	Shanghai Sunny Hengping Scientific Instrument Co., Ltd.
X-ray diffraction analyzer	Bruker D8 A25	Brock Co. Ltd.
X-ray photoelectron spectrometer	Kratos AXIS Ultra DLD	Kratos Co. Ltd.
Specific surface area tester	ASAP 2020	Micromeritics Instrument Co. Ltd.
Fourier Transform Infrared Spectrometer	Bruker V70	Brock Co. Ltd.
Transmission electron microscope	JEM 2100	JEOL Co. Ltd.

3.4 Preparation of catalysts

Mo-Mn catalysts were synthesized by the incipient wetness impregnation (IWI) method. The mesoporous γ -Al₂O₃ was used as the support: (NH₄)₆Mo₇O₂₄•4H₂O and Mn(NO₃)₂•4H₂O (Sino-pharm Chemical Reagent Co, Ltd) were used as the precursors. In this study, the MoMn/ γ -Al₂O₃ catalysts with 2,4,6 wt% of Mn-loading were prepared. The detailed processes for sample production were recommended elsewhere[42]. Metal precursors, such as Cu(NO₃)₂•6H₂O and (NH₄)₆Mo₇O₂₄•4H₂O, were dissolved in deionized water. IWI prepared CuO/ γ -Al₂O₃ and CuMoO/ γ -Al₂O₃. After calcination, CuS/ γ -Al₂O₃ and CuMoS/ γ -Al₂O₃ were prepared by the sulfurization of CuO/ γ -Al₂O₃ and CuMoO/ γ -Al₂O₃ via sulfur-chemical vapor reaction (S-CVR) method.

3.5 Hg⁰ removal experiments

3.5 Hg⁰ removal experiments

The demercuration performance was studied by qualitative and quantitative analysis, while the demercuration performance of catalysts was measured via temperature-programmed surface reaction (TPSR). The catalyst's performance in terms of adsorption and catalytic oxidation of Hg⁰ was tested under 30°C~700°C dynamic temperature-programmed experiment conditions. The removal effect of Hg⁰ was probed via qualitative analysis, while the catalytic oxidation effect of Hg⁰ was studied via quantitative analysis. All reactions use air as carrier gas and the proportion of oxygen(5%) is regulated by the addition of nitrogen. The catalyst should be dried in an oven(120°C) before use to avoid the interference of water on the experiment.

A special experimental device was designed to test the Hg⁰ catalytic removal effect with prepared specimens. The mercury producer (Tekran 3310, USA) inside the machine generated certain amounts of Hg⁰ within a given time. And mercury analysis system (Tekran 3300RS, USA) continuously calculated the amount of mercury (Hg^T), Hg²⁺ that was shown as $[Hg^{2+}] = [Hg^T] - [Hg^0]$. Therefore, the data of Hg⁰ catalytic oxidation with the different catalysts can be well recorded for later analyses with an

integrated dynamic-state experimental method to be used to get the maximum instantaneous mercury removal efficiency (ΔX_{max}) and catalytic oxidation rate.

The maximum instant mercury removal efficiency ΔX_{max} and Catalytic Oxidation Ration can be calculated by following equations[42].

$$\Delta X_{max} = \frac{[Hg^0]_{in} - [Hg^0]_{out}}{[Hg^0]_{in}} \times 100\% \quad (1)$$

$$\text{Catalytic Oxidation Ration} = \frac{Hg^{2+}}{[Hg^0]} \times 100\% \quad (2)$$

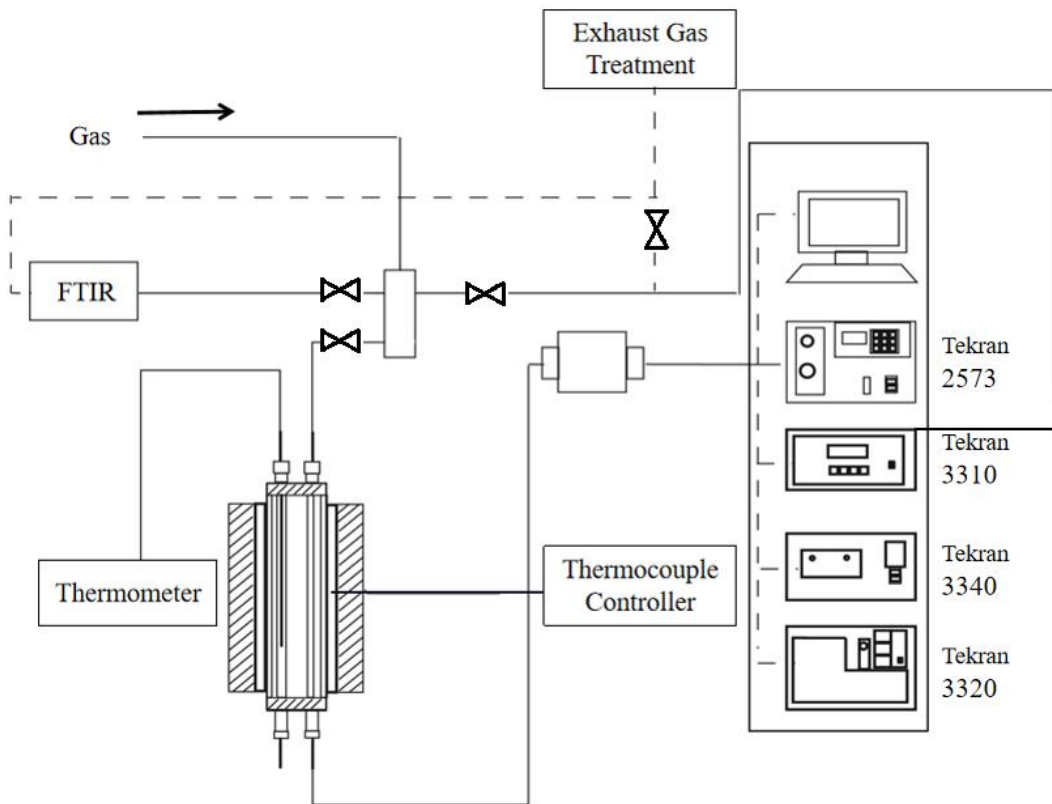


Figure. 1 Schematic diagram of the experimental system

Chapter 4 Performance of Mn/Mo-Mn catalyst in Hg⁰ removal

4.1 Analysis of Hg⁰ removal efficiency

4.1.1 Evaluation of Hg adsorption and catalytic oxidation performance

The Hg⁰-TPSR results for different concentrations of Mn promoted by 1.25% Mo have been shown in Figure 3. Based on Figure 2 and 3, the characteristic temperatures have been concluded in Table 2, including the initial adsorption temperature (T_{a0}), the adsorption rate peak ($T_{ra, \text{ peak}}$), the best effective adsorption range ($T_a, \text{ range}$), the initial desorption temperature (T_{d0}) and the desorption rate peak ($T_{rd, \text{ peak}}$).

T_{a0} was an indicator related to catalyst activity. To some extent, it had a strong connection with activation energy. 1% Mn had the highest initial adsorption temperature, which was 69.4°C. Then, T_{a0} decreased 25.5°C gradually with an increase in the Mn concentration. The trend for T_{a0} change was applicable for both Mn oxides and Mo-promoted Mn oxides. If we compared T_{a0} of Mn oxides with Mo-promoted Mn oxides, it can be found that T_{a0} for Mo-promoted Mn oxides was much higher than oxides of the same concentration of Mn. Thus, it could be concluded that the increase of Mn would cause deterioration in T_{a0} and the dope of 1.25%Mo would increase T_{a0} notably.

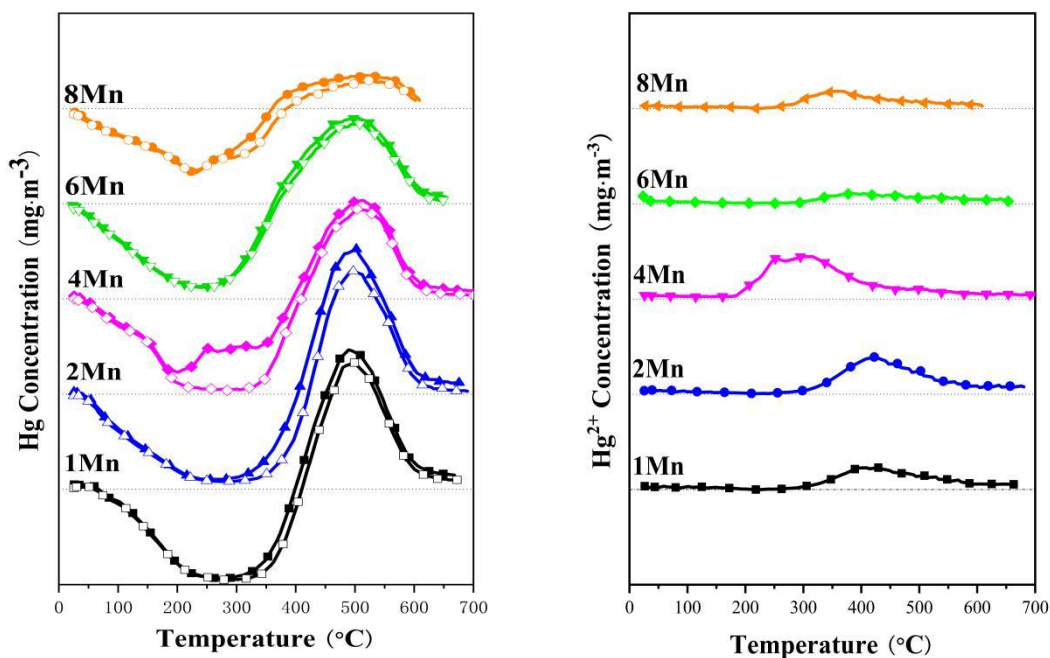


Figure 2. Hg^T and Hg⁰ (a) and Hg²⁺(b) dynamic transient-state analysis of Mn catalysts with ranges of Mn loadings.

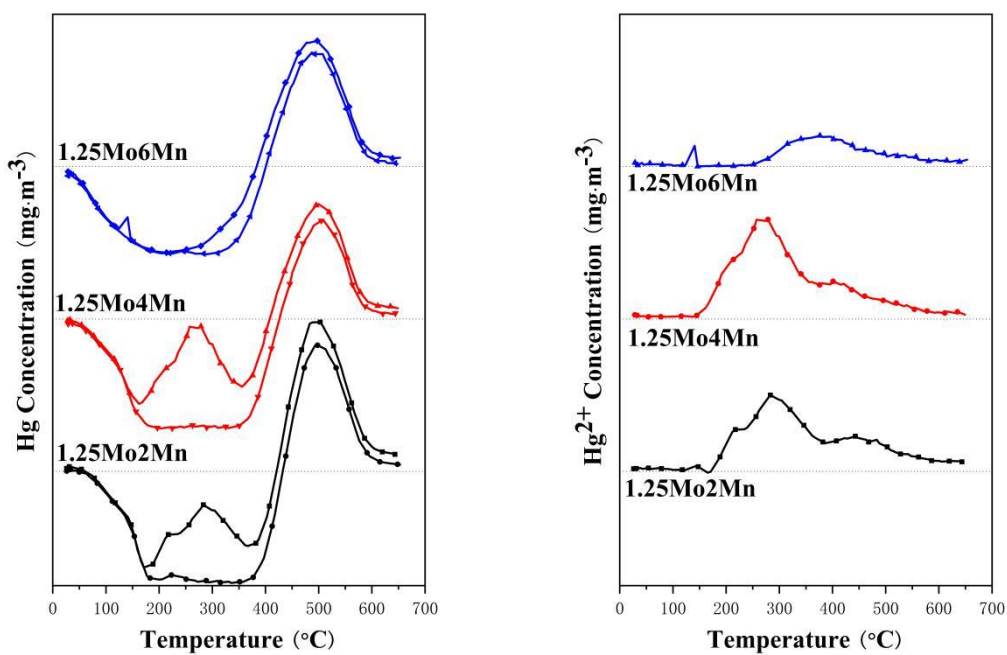


Figure 3. Hg^{T} and Hg^0 (a), Hg^{2+} (b) dynamic transient-state analysis of Mn-Mo catalysts with ranges of Mn loadings.

Table 2. Characteristic temperatures of Mn oxides and Mo-promoted Mn oxides.

Sample	T_{a0} (°C)	$T_{ra,peak}$ (°C)	$T_{a,range}$ (°C)	T_{d0} (°C)	$T_{rd,peak}$ (°C)
1Mn	69.4	183.9	278.8	409.2	419.1
2Mn	45.8	67.6	293.1	407.1	437.3
4Mn	41.3	172.3	212.7-326.6	398.5	443.8
6Mn	31.2	148.4	240	362	367
8Mn	25.5	190.5	228.5	365.5	396.3
1.25Mo2Mn	63.2	159.4	177-376.9	433.1	433.1
1.25Mo4Mn	62.6	133	173.9-350.6	426.1	445.8
1.25Mo6Mn	48.6	70.3	180.7-330.5	407.3	407.3

4.1.2 Quantitative analysis for evaluating Hg^0 catalytic oxidation

The activation energy of Hg^{2+} and Hg^0 capture process for Mn oxides and Mn oxides promoted by 1.25% Mo were also recorded in this study. The results were listed in Table 2. The R^2 values for all Mo-promoted Mn oxides exceeded 0.94, indicating a good fit to Arrhenius equation. The values of E_a for 1.25% Mo-promoted Mn oxides were recorded in the third column of Table 3. According to the calculation, the value

of E_a of 1.25%Mo6%Mn was lower than the original Mn oxides by at least 17%. The activation energy for 1.25%Mo2%Mn and 1.25%Mo4%Mn was also reduced by approximately 50% and 32% respectively. These data directly showed that adding Mo had a positive effect on their Hg^0 and Hg^{2+} capture performance in terms of reducing activation energy. This characteristic will allow the mercury capture process to occur at a relatively lower temperature and save energy. Among the group of Mn samples with Mo loading, 1.25%Mo4%Mn samples had shown the lowest activation energy compared with the other two Mo-loading samples. While the 1.25%Mo6%Mn had the highest activation energy among all the three.

The ΔX_{max} region was in a best position to evaluate indicators of mercury removal rates directly. The max for each concentration was recorded (Table 3). The order of maximum Hg^0 removal efficiency from high to low was 1.2%5Mo2%Mn (98% at 336°C) > 1.25%Mo4%Mn (96% at 202°C) > 1.25%Mo6%Mn (75% at 289°C). Combined activation energy with removal rate, the 1.25%Mo2%Mn and 1.25%Mo4%Mn sample demonstrated the high mercury removal rate.

Table 3. Summary of reaction kinetics for Mn oxides and Mn oxides promoted by 1.25%Mo

Sample	Slope	E_a (kJ/mol)	R^2	ΔX_{max} (%)
1Mn	-10222	85.0	0.80 7	95
2Mn	-7443	61.9	0.98 6	92
4Mn	-5514	45.8	0.97 5	96

6Mn	-6196	51.5	0.92	88
			1	
8Mn	-7419	61.7	0.80	66
			6	
1.25Mo2Mn	-4081	33.9	0.96	98
			2	
1.25Mo4Mn	-3729	31.0	0.97	96
			2	
1.25Mo6Mn	-5109	42.5	0.94	75
			9	

Table 4. Catalytic capacity analysis for Mn oxides and Mn oxides promoted by 1.25Mo.

Sample	S _a (min μg/m ³)	S _d (min μg/m ³)	ΔS (min μg/m ³)	S _{Hg2+} (min μg/m ³)	Ratio (%)
2Mn	3524.95	2366.82	1158.14	1135.13	32.2
4Mn	3318.37	1903.80	1414.57	1459.42	42.6
6Mn	2634.78	2113.42	521.35	426.61	19.8
1.25Mo2Mn					
n	3973.53	1692.72	2280.80	2254.20	57.4
1.25Mo4Mn					
n	3749.04	1434.04	2314.99	2312.81	61.7

1.25Mo6M			821.82	808.81	29.2
n	2816.06	1994.24			

The relative absorption capacity (Sa), relative desorption capacity (Sd) and their difference (ΔS) were used to assess the Hg^0 and Hg^{2+} capture ability because Hg^0 and Hg^{2+} were speculated to be captured in the form of [Hg-O] at the surface of Mn oxides.[42] The results were summarized in Table 4. It can be seen that both relative absorption capacity and ΔS decreased with more Mn proportion. 4Mn had the highest catalytic oxidation and the lowest relative desorption capacity. Compared with the Mn oxides, Mn oxides promoted by 1.25Mo had larger relative absorption capacity and even lower relative desorption capacity, causing larger ΔS . This indicated that the addition of 1.25 Mo could improve the efficiency of the catalyst in all aspects.

4.2 Characterization

4.2.1 XRD

To analyze the crystallization and monolayer coverage of each catalyst, we investigated XRD patterns for a series of Mn and Mo-adjusted Mn-based bimetallic catalysts at different loadings on $\gamma-Al_2O_3$ support. Generally, the $\gamma-Al_2O_3$ support's characteristic peaks can be found in XRD pattern (Figure 4) at 37.5° , 46.5° and 67.2° respectively. The intensity of these peaks decreased as the Mn loading increased. This indicated that a higher amount of Mn could result in stronger interactions between Mn and $\gamma-Al_2O_3$ [39]. The remaining peaks indicated that the dopant Mn had formed crystals on the catalyst surface. The increase of MnOx doping amount in MnOx/ $\gamma-Al_2O_3$ catalysts resulted in the presence of the diffraction peaks of MnO_2 , MnO and Mn_2O_3 in the XRD patterns of 4Mn/ $\gamma-Al_2O_3$ and 6Mn/ $\gamma-Al_2O_3$. This could be attributed to the formation of MnOx crystallites on the Mn-rich catalysts. According to the peak location, MnO_2 belonged to $\beta-MnO_2$ and $\delta-MnO_2$. $\delta-MnO_2$ contributed to the catalytic oxidation of mercury. MnOx crystal structures assembled on the support might cause a certain effect on the absorption performance of catalysts.

The highest crystallinity of MnOx occurred at 6Mn/ γ -Al₂O₃ samples. Although more MnOx crystal structures may block the formation of MnOx monolayer coverage and reduce absorption performance, it showed a high catalytic oxidation ability. This also explained that the catalytic oxidation efficiency of Mn catalyst increased as the Mn content increased. However, the further increase of the dopant cannot be distributed better on the surface of the carrier, making the required activation energy increase and catalytic oxidation efficiency decrease.

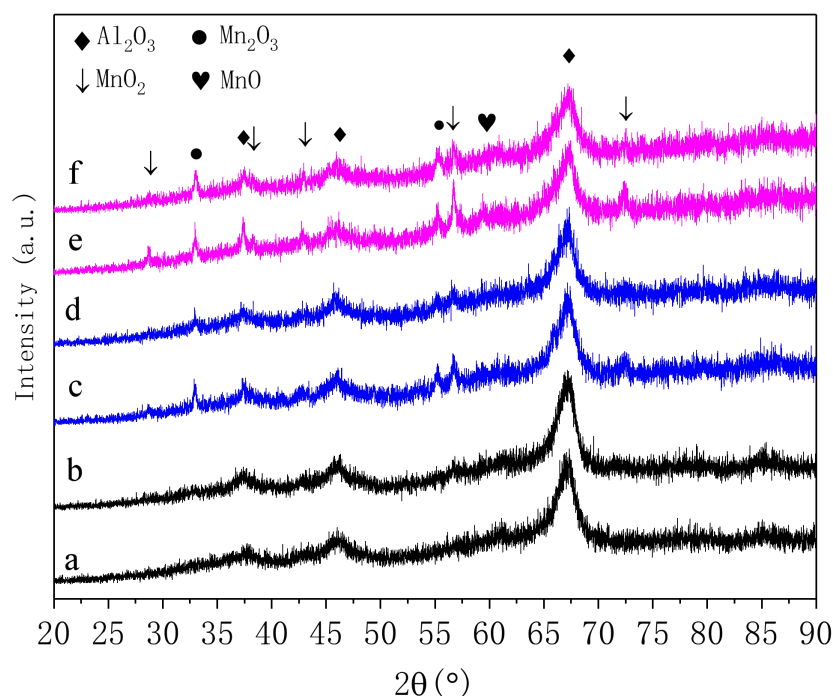


Figure 4. XRD patterns of catalysts a. 2Mn/ γ -Al₂O₃, b. 1.25Mo2Mn/ γ -Al₂O₃, c. 4Mn/ γ -Al₂O₃, d. 1.25Mo4Mn/ γ -Al₂O₃, e. 6Mn/ γ -Al₂O₃, f. 1.25Mo6Mn/ γ -Al₂O₃.

By comparing the samples before and after Mo doping, we found that the weak diffraction peaks of MnO₂, MnO and Mn₂O₃ in the XRD patterns, and the addition of Mo slightly decreased the intensity of the diffraction peaks. This illustrated the lower weak peak intensity, indicating that the active components were distributed more evenly over the sample because of the addition of Mo. Therefore, by considering these two significant aspects, we found that the 1.25Mo4Mn sample had good monolayer coverage and catalytic oxidation ability. This result also matched the

Hg⁰-TPSR results shown in Figure 2. Adding 1.25Mo can promote the formation of catalyst monolayer coverage and efficiency.

4.2.2 BET

The effect of modified Mo-based catalysts with a different Mn ratio on the surface, volume of resources and width of catalyst resources was further evaluated. Results for Mn and Mo-Mn catalysts combined were shown in Figure 5.

As it can be seen from Figure 5, with the increase of Mn content, the specific surface area of 4Mn and 6Mn catalyst decreased significantly, because the crystalline MnO_x increased with the rise of Mn content. Similar trends were observed in the specific surface and volume of pores in the sample. This was mainly because the metal oxide was supported on the surface of Al₂O₃, and the growth and establishment of nanoparticles led to the formation of crystals under the heavy manganese load. The specific surface of the crystal structure was generally smaller than that of the amorphous structure, which obstructed the pores and led to the decrease of the surface and total volume of pores. This was typical of the impregnation process.

However, when 1.25Mo was added to the Mn catalyst, all samples were optimized to a different degree. 1.25Mo4Mn showed the largest change, and the specific surface area increased by more than 30%, which was higher than other samples. This revealed that the catalyst 1.25Mo4Mn had the highest activity among these samples, which also explained the reason for the high mercury removal capacity of 1.25Mo4Mn.

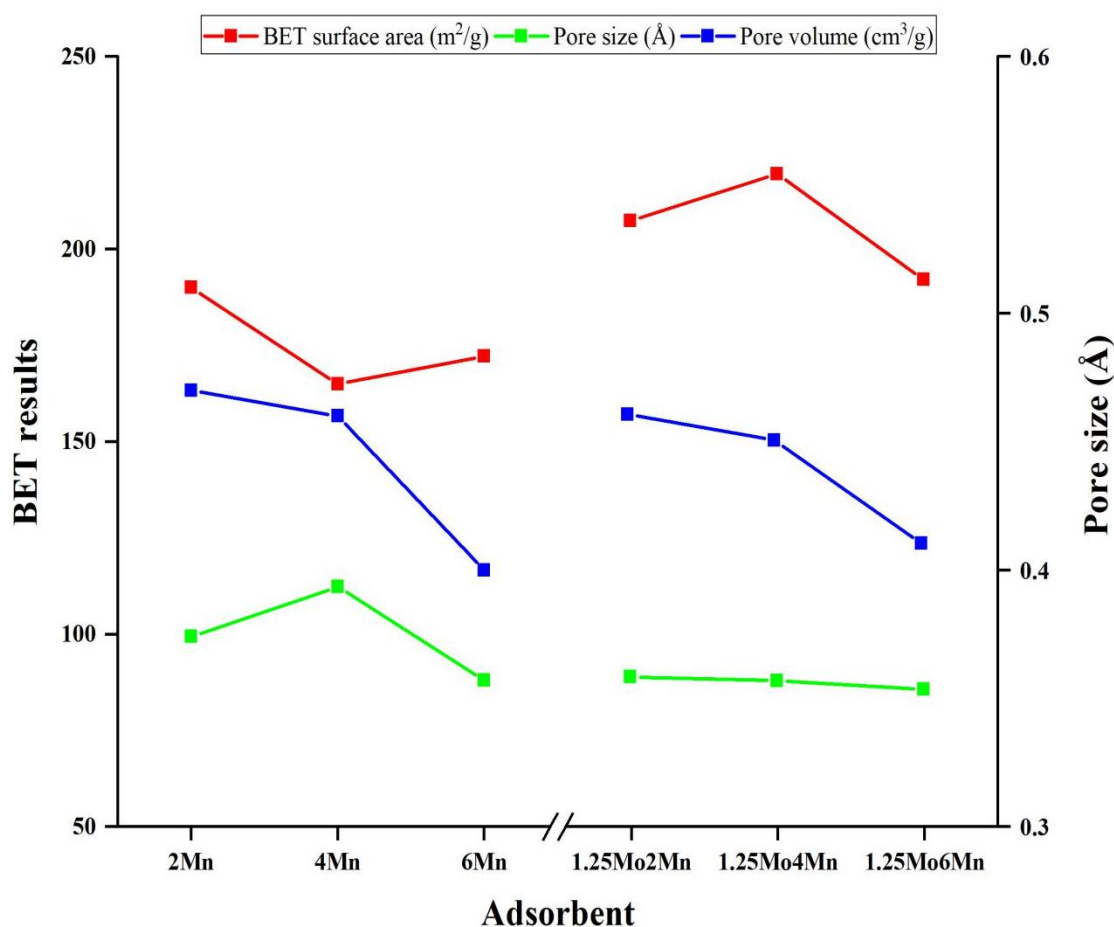


Figure 5. The surface properties of Mo catalysts with different ratios of Mn

4.2.3 TEM

For the purpose of studying the morphology and structure characteristics of catalysts, TEM and HRTEM were used to characterize 4Mn and 1.25Mo4Mn catalysts(Figure 6). TEM images in Figure 6(a.) and (b.) can clearly observe the layered structure, indicating that MnO₂ components were well dispersed on the surface of the γ -Al₂O₃ carrier, which was the same with the XRD analysis.

The HRTEM image in Figure 6(c.) clearly showed a well-crystallized δ -MnO₂(110) lattice plane with a spacing of 0.41nm. After Mo was added, no molybdenum oxide with clear lattice spacing was found in Figure 6(d.), indicating that MoO_x spread evenly over the catalyst's surface..

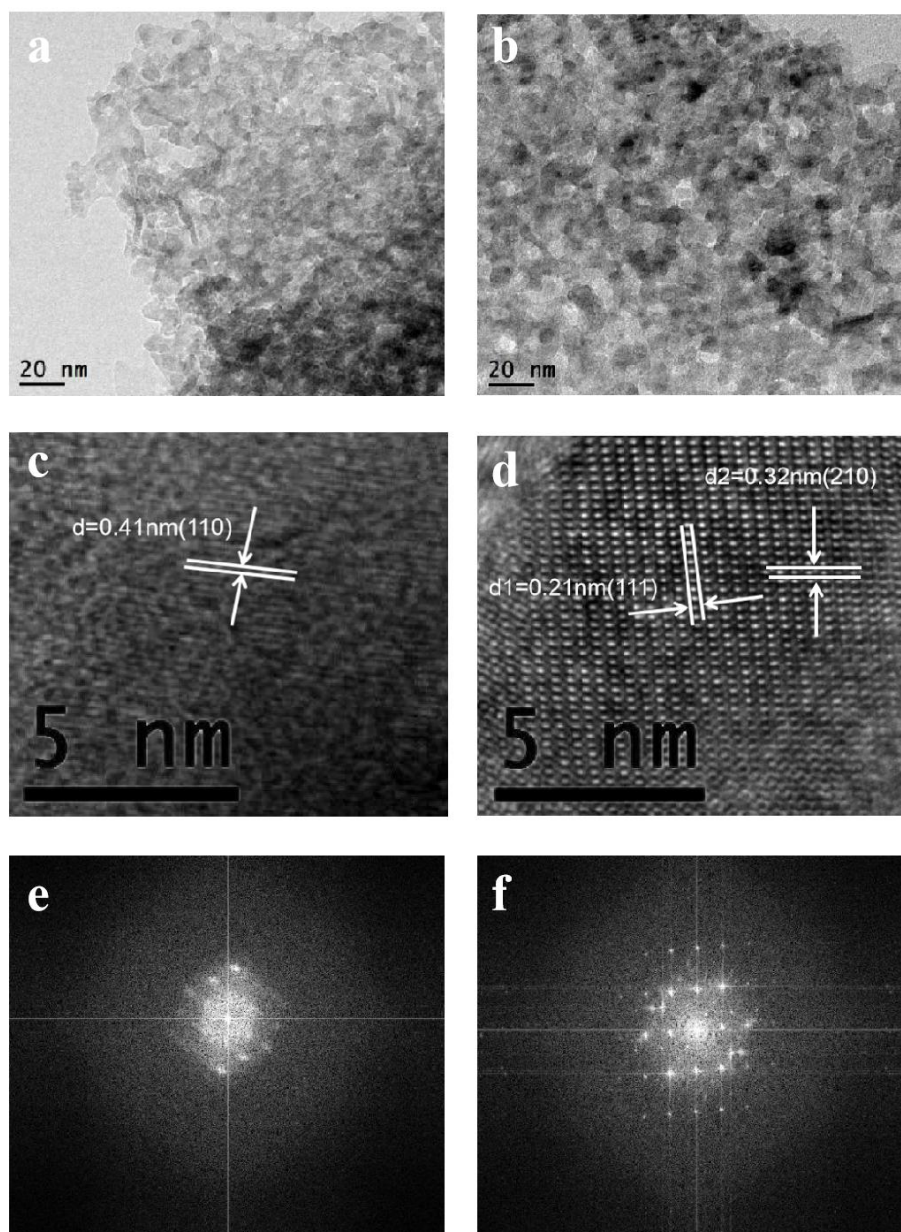


Figure 6. TEM images of a.1.25Mo4Mn/ γ -Al₂O₃ catalyst, b.4Mn/ γ -Al₂O₃ catalyst; HRTEM image of c.1.25Mo4Mn/ γ -Al₂O₃ and d.4Mn/ γ -Al₂O₃; FFT view of the c.1.25Mo4Mn/ γ -Al₂O₃ catalyst and f.4Mn/ γ -Al₂O₃.

Besides, no relevant particle lattice was observed, indicating poor crystallinity, which may be due to the presence of MoO_x, which enhanced the interaction between Mn and Al₂O₃ carrier and affected its crystallization. This explained that the diffraction peak intensity of MnO₂ decreases under the influence of Mo(Figure 4). In Figure 6

(d.), it was found that the (111) and (210) crystal planes of MnO_2 overlapped, (111) crystal plane was above (210) crystal plane, with an overlap angle of 80 degrees. From Figure 6(d.), it can be confirmed that the two active components overlap. This indicated that Mo ions with a large ionic radius were added to the Mn lattice, resulting in crystal surface overlap, which may produce more active sites at the interface, thus improving the catalytic effect of Hg^0 .

4.2.4 DRIFT

In order to further study the influence of acidic sites on catalytic performance, we used NH_3 as a molecular probe in DRIFT. Previous literature showed that the catalytic oxidation of Hg^0 was positively correlated with the number of Brønsted acid sites on the catalyst surface because Hg^0 can be seen as a base.

Figure 7 showed a semi-quantitative analysis of Brønsted acid and Lewis acid ratios, which was the integrated area for in-situ DRIFT of 4Mn, 1.25Mo2Mn, 1.25Mo4Mn and 1.25Mo6Mn catalyst at different temperatures. Combined with the analysis of Hg-TPSR, it can be found that the catalyst with a high B/L acid site ratio had higher catalytic oxidation efficiency. Besides, the the catalyst at temperature (150°C) with the highest B/L acid site ratio in 1.25Mo2Mn was higher than other catalysts. This can also explain the 1.25Mo2Mn catalyst activity temperature slightly higher than other catalysts.

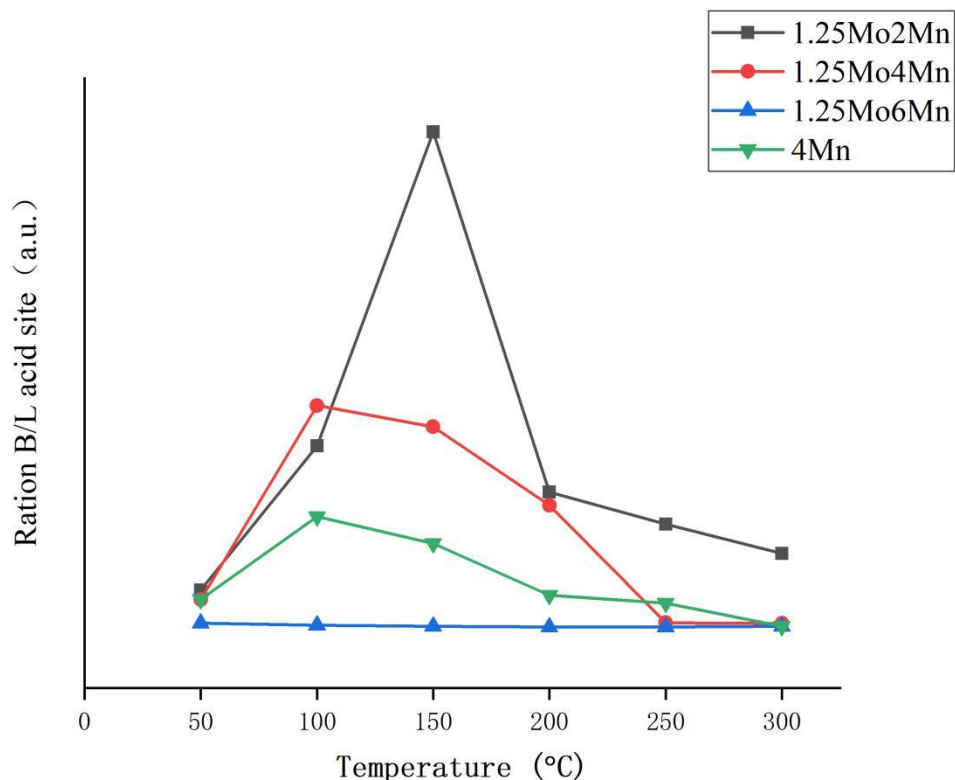


Figure 7. *In-situ* DRIFT study of surface acid sites for FTIR of NH_3 on $4\text{Mn}/\gamma\text{-Al}_2\text{O}_3$, $1.25\text{Mo}2\text{Mn}/\gamma\text{-Al}_2\text{O}_3$, $1.25\text{Mo}4\text{Mn}/\gamma\text{-Al}_2\text{O}_3$ and $1.25\text{Mo}6\text{Mn}/\gamma\text{-Al}_2\text{O}_3$ catalysts.

4.3 Summary

In this chapter, $\text{MnO}_2/\gamma\text{-Al}_2\text{O}_3$ and $\text{MnO}_2\text{-MoO}_3/\gamma\text{-Al}_2\text{O}_3$ catalysts with different Mn loading ratios were prepared by the same volume impregnation method. The mercury removal effects of catalysts were studied from the qualitative and quantitative perspectives through the temperature-programmed surface reaction (TPSR). The relationship between the structure, composition and reaction activity of the catalysts by different characterization methods was studied.

(1) In single metal Mn catalyst and MnMo bimetallic catalyst, when the Mn loading was 4%, $4\% \text{Mn}/\gamma\text{-Al}_2\text{O}_3$ and $1.25\% \text{Mo}4\% \text{Mn}/\gamma\text{-Al}_2\text{O}_3$ had the best catalytic effect. Dynamic analysis showed that $4\% \text{Mn}/\gamma\text{-Al}_2\text{O}_3$ had the best catalytic oxidation effect when the temperature was around 275°C . When Mo entered the catalyst as a dopant,

the 1.25%Mo4%Mn/ γ -Al₂O₃ catalyst can achieve the best catalytic oxidation efficiency (96%) at 202 °C.

(2) XRD analysis showed that the pre-doping of Mo was conducive to the distribution of MnO_x on the carrier. This was consistent with the result of the representation of BET. Meanwhile, with the addition of Mo, the BET Surface area was greatly increased. This indicated that with the addition of Mo, the activity of the catalyst was greatly enhanced. TEM can clearly observe that with the addition of molybdenum, the two layers of crystal surface overlapped, which provided more active sites for the catalyst. According to DRIFT analysis, there were more acidic sites on the surface of the Mo-Mn bimetallic catalyst, which was conducive to the adsorption of Hg⁰.

Chapter 5 Performance of Cu-S/Cu-Mo-S adsorbent in Hg⁰ removal

5.1 Hg⁰ removal efficiency analysis

5.1.1 Dynamic transient screening of adsorbents

For the purpose of selecting the best performance of CuS and CuMoS adsorbents among different Cu loadings, the dynamic transient screening method was used, and the results were presented in Figure 8 and Figure 9 respectively. The capture performance of adsorbents was evaluated and results were shown by following Figure 8. In this experiment, four groups of CuS containing adsorbents with different copper loading amounts (from 2%wt to 8%wt) were tested. It was obvious that the adsorption performance of four groups were almost the same, all of which had an efficiency higher than 95% before the temperature reached 70 °C. After 70°C, all adsorbents started lost their efficiency gradually. It was about 135°C the 2wt% Cu-loading adsorbent achieved the removal efficiency of 10%. This could be roughly concluded that the maximum CuS containing adsorbents absorbing temperature should not exceed 135°C. Among these adsorbents, the 4%wt Cu-loading adsorbent had a broader effective temperature window compared with the other three groups (remained higher than 90% efficiency between 70°C and 115°C). It was obvious that while four groups of adsorbents had nearly the same mercury removal efficiency below 70 °C but 4%wt-Cu had the advantage of a wider effective temperature range.

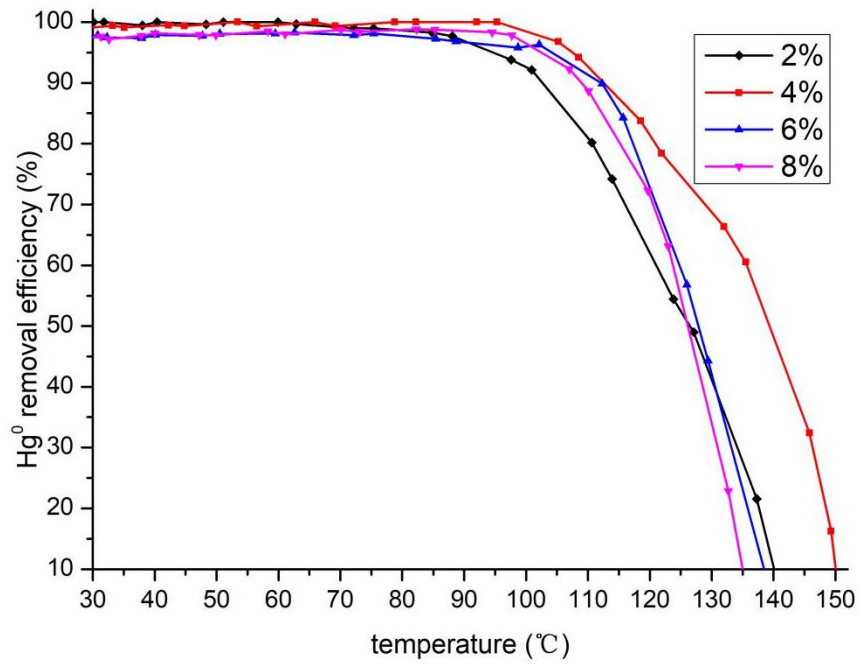


Figure 8. Results of dynamic transient screening of CuS adsorbents at 2wt%, 4wt%, 6wt% and 8wt% for Hg^0 capture (concentration: $30\mu g/m^3$).

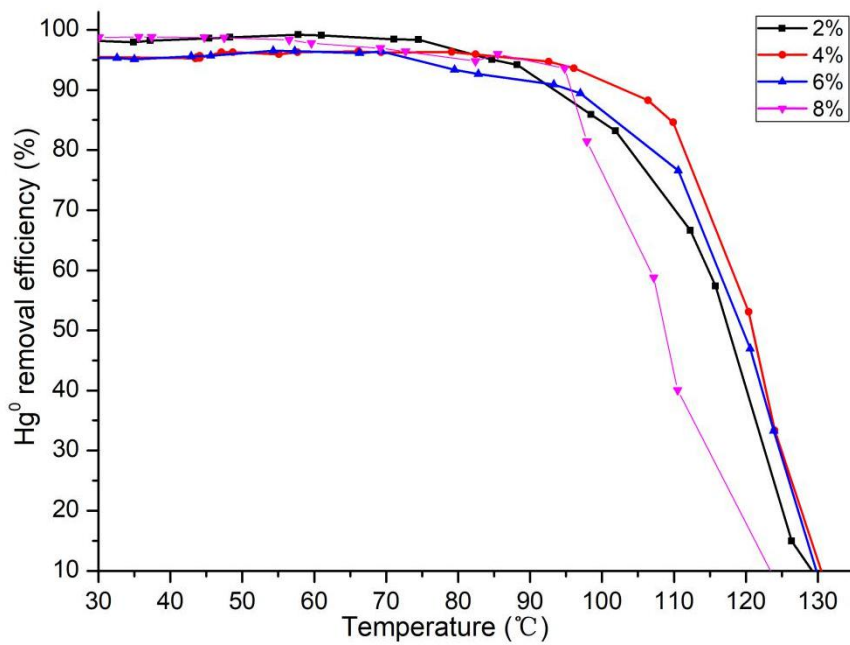


Figure 9. Results of dynamic transient screening of CuMoS adsorbents at 2wt%,

4wt%, 6wt% and 8wt% for Hg^0 capture (concentration: $30\mu g/m^3$).

Figure 9 showed the capture performance of CuMoS adsorbents with different Cu-loading. It was conspicuous that adsorbents with 2wt% Cu-loading and 4wt% Cu-loading showed a perfect mercury removal performance within $100^\circ C$, 6wt% Cu-loading and 8wt% Cu-loading showed slightly low efficiency. Moreover, all of them had a steady efficiency higher than 95% at the temperature range of $30^\circ C$ - $100^\circ C$. With the increase of temperature, the activity of all CuMoS began to decrease gradually. All of them were below the 10% removal efficiency at $150^\circ C$. Among these adsorbents, 4wt% Cu-loading also showed a broader effective temperature window ($30^\circ C$ - $150^\circ C$). It had both advantages of excellent adsorption ability and remaining active in a wider temperature range. Therefore, adsorbents of CuS and CuMoS with 4% Cu-loading were chosen and used as the most promising mercury capture adsorbents for further research.

5.1.2 Steady-state evaluation

Based on the dynamic transient screening, steady-state evaluated the temperature range of adsorbents effective in mercury capture. The range was from 25 to $150^\circ C$, and results were recorded as diagrams which were shown in Figure 10 and Figure 4 respectively. Figure 10 clearly revealed that the CuS adsorbent removal efficiency remained higher than 95% when the temperature was lower than $100^\circ C$, but dropped to approximately 80% and 60% when the temperature reached $125^\circ C$ and $150^\circ C$ respectively. Among these groups' temperature were below $100^\circ C$, the efficiency in mercury capture increased gradually while the temperature increased; until $75^\circ C$, the mercury capture efficiency reached the peak efficiency of 97%. After that, the efficiency started to decrease gradually to approximately 95% at $100^\circ C$.

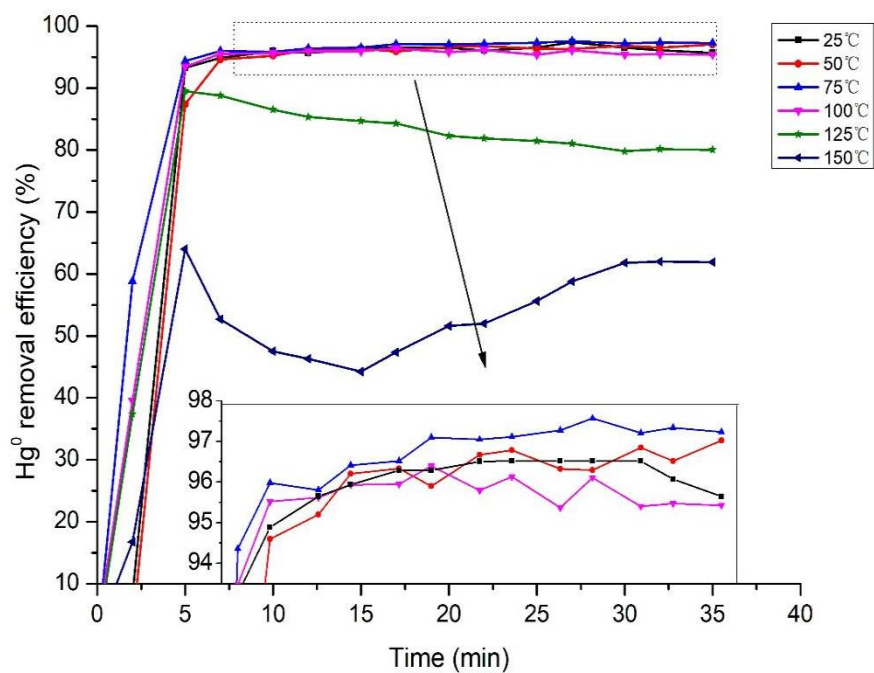


Figure 10. Results of steady state evaluation of adsorbent doped with 4wt% CuS (Hg^0 concentration: $30\mu g/m^3$)

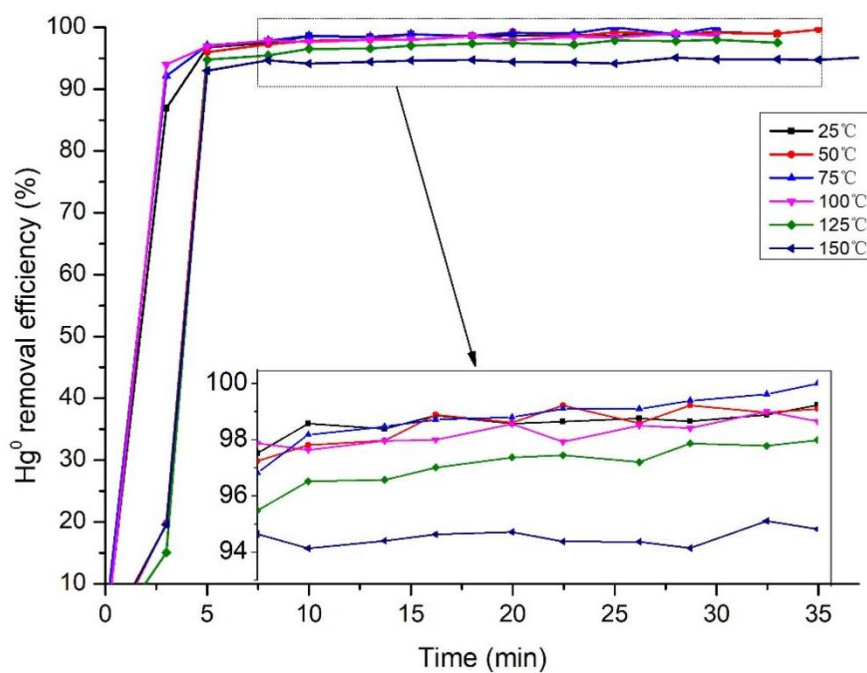


Figure 11. Results of steady-state evaluation of adsorbent doped with 4wt% CuMoS (Hg^0 concentration: $30\mu g/m^3$)

In Figure 11. The efficiency of CuMoS adsorbent could maintain above 96% when the temperature was lower than 100°C and slightly dropped to 94% when the

temperature reached 150°C. The efficiency among adsorbents was continuously increasing till the temperature approached 75°C, then decreased gradually as the temperature continued increasing. Adsorbents at 75°C showed the peak value of efficiency and had a slightly better performance of mercury capture. This result showed that both CuS and CuMoS adsorbent had a best performance temperature of 75°C. However, there was no significant drop in CuMoS adsorbent capture efficiency when the temperature was higher than 100°C comparing with CuS adsorbent. Therefore, the temperature range around 75°C could be concluded as the most suitable temperature for CuS and CuMoS adsorbents to present better performance of mercury capture. The addition of Mo could promote the ability of adsorbent at high temperatures.

5.1.3 Space velocity analysis

From Figure 12, the WHSV of $2.2 \times 10^3 h^{-1}$ achieved the highest, approximately 96% of mercury removal efficiency. By contrast, the efficiency had slightly decreased when the WHSV increased to $2.6 \times 10^3 h^{-1}$ at the initial state, but it then increased to 95% after 50min. When the WHSV was further increased to $4.0 \times 10^3 h^{-1}$, the efficiency dropped to 92.5%. This indicated that the adsorbent would lose part of efficiency when the space velocity was high, because high velocity could reduce the time of gas diffusion and reaction with adsorbents. The results suggested that the WHSV raised to above $2.6 \times 10^3 h^{-1}$ could maintain the high mercury capture performance, and a significant drop in capture efficiency occurred when the WHSV increased to $4.0 \times 10^3 h^{-1}$.

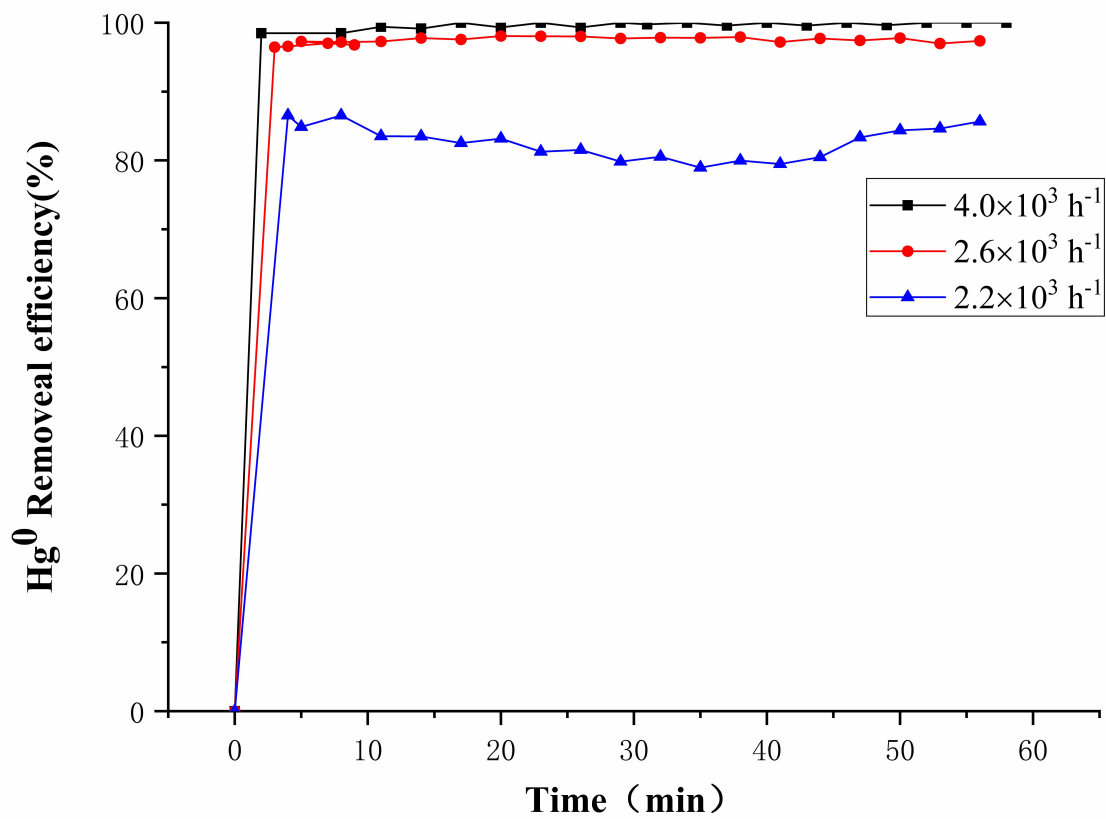


Figure 12. CuS adsorbent Hg⁰ capture performance at different space velocity scenarios

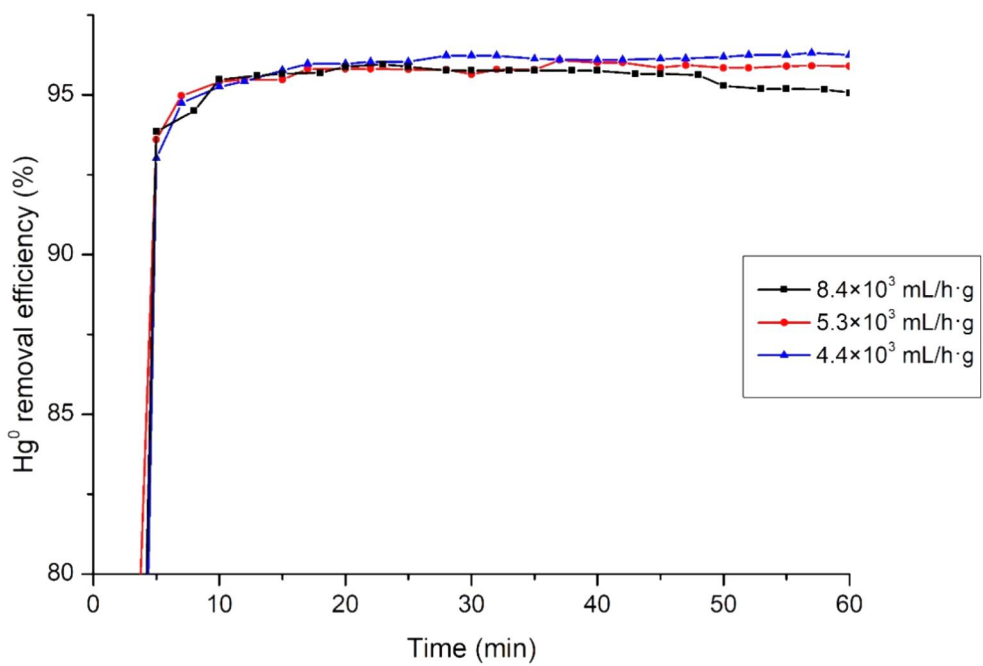


Figure 13. CuMoS adsorbent Hg⁰ capture performance at different space velocity scenarios

Figure 13 revealed that at the initial state, the growth trend of three data was the same and intertwined. After 30 mins, data segregated and showed a clearly varied trend. The efficiency of WHSV of $4.4 \times 10^3 h^{-1}$ reached 96%, but that of WHSV of $8.4 \times 10^3 h^{-1}$ dropped to 95%. The WHSV of $5.3 \times 10^3 h^{-1}$ maintained the removal efficiency above 95%. These results showed that the reverse relationship was that high space velocity led to low mercury removal efficiency and suggested that the high mercury removal efficiency could be achieved when the space velocity was $5.3 \times 10^3 h^{-1}$. If the space velocity increased to $8.4 \times 10^3 h^{-1}$, it might cause a performance drop.

5.2 Characterization

5.2.1 XRD

To test the crystallization and monolayer coverage on the surface of the adsorbents, we used the X-Ray diffraction method. In this experiment, the CuS and Mo-loading CuS adsorbents with different Cu quantities were investigated. The XRD patterns were shown in Figure 9. It was conspicuous that Al_2O_3 characteristic intensity peaks were located at 38.5° and 68.5° and the peak at 46° represented both Al_2O_3 and Cu_2S . Points 20° , 34.5° and 44.5° showed very mild intensity of Al_2O_3 and Cu_2S existence. By comparing the differences among quantities in Figure 14, we found a mild decrease among Cu_2S characteristic intensity peaks. This indicated that the addition of Mo could affect the Cu_2S crystal structure formed on the surface of adsorbents. Cu_2S had higher heat-resistance chemical properties than Cu^{2+} . This explained the results shown in Figure 8 and Figure 9. Comparing the peak between CuS and Mo-loading CuS adsorbents, we found that Cu_2S intensity peaks of CuMoS as presented in these patterns were slightly higher than those of CuS adsorbents. The Cu^{2+} was transformed to Cu^{1+} as the result of CuMoS formation. Therefore, the amount of Cu_2S increased.

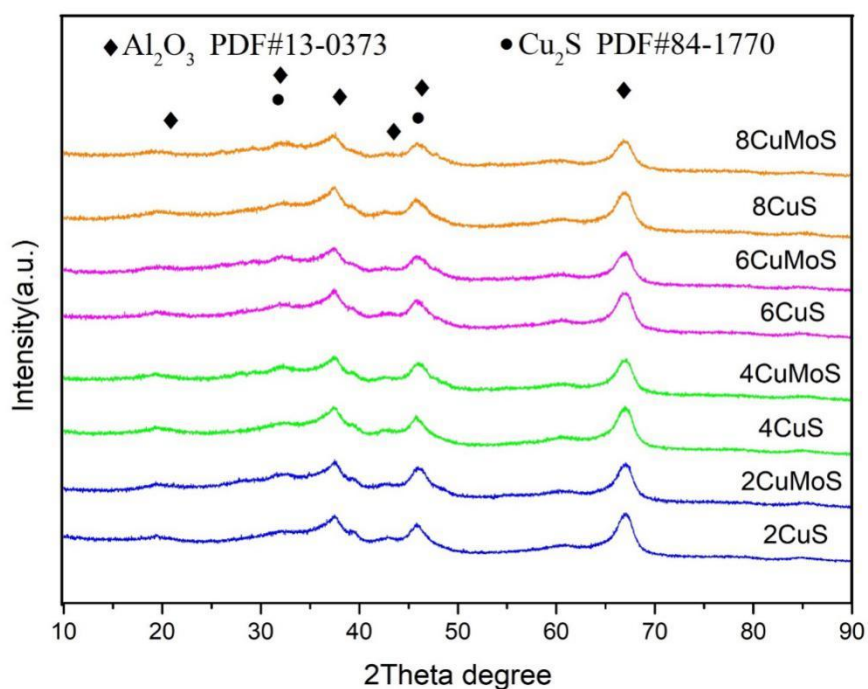


Figure 14. XRD patterns of CuS adsorbents before and after Mo modified

5.2.2 XPS

The XPS spectrum of Cu 2p presented the chemical states[53] of both Cu^+ (932.2eV and 952.1eV for Cu $2p_{3/2}$ and $2p_{1/2}$) and Cu^{2+} (934.13V and 954.2eV for Cu $2p_{3/2}$ and $2p_{1/2}$). However, peaks of Cu compounds were almost immobile in the XRD pattern of 4%CuS/ γ - Al_2O_3 . The reduced copper was present in the sample for amorphous. For 4%CuMoS/ γ - Al_2O_3 (Figure b), the satellite peak almost disappeared, indicating that a small amount of Cu^{2+} in the sample was reduced to Cu^{1+} to form Cu_2S [54]. These univalent copper adsorbents provided better thermal stability, which was consistent with the results of XRD and Hg-TPSR analysis.

As to the spectrum of Mo 3d, Figure C showed that the two main peaks of Mo were centered on 236eV and 232.8eV respectively. These two peaks belonged to Mo^{6+} . Also, the Mo^{4+} was present in 4%CuMoS/ γ - Al_2O_3 (293.28eV for Mo $3d_5$)[55]. With the addition of Mo, the conversion was more from Cu^{2+} to Cu^+ . This should be the reason for the disappearance of the satellite peak for Cu^{2+} in 4%CuMoS/ γ - Al_2O_3 .

The XPS spectrum of S2p₃ in 4%CuS/γ-Al₂O₃ and 4%CuS/γ-Al₂O₃ was almost identical. The peaks around 160–166eV showed the typical values for sulfide (S²⁻, 161.9eV and 163.1eV for 2p_{3/2} and 2p_{1/2}, respectively) and disulfide ((S₂)²⁻, 164.0eV and 165.2eV for 2p_{3/2} and 2p_{1/2}, respectively)[56]. Their corresponding product would be CuS, Cu₂S and MoS₂.

Cu-S has been verified as an excellent adsorbent to reduce Hg in Cu and S co-impregnated activated carbon[57]. CuS/ γ -Al₂O₃ adsorbents' and CuMoS/ γ -Al₂O₃ adsorbents' main adsorption capacity comes from Cu-S. The addition of Mo led to the generation of more active sites.

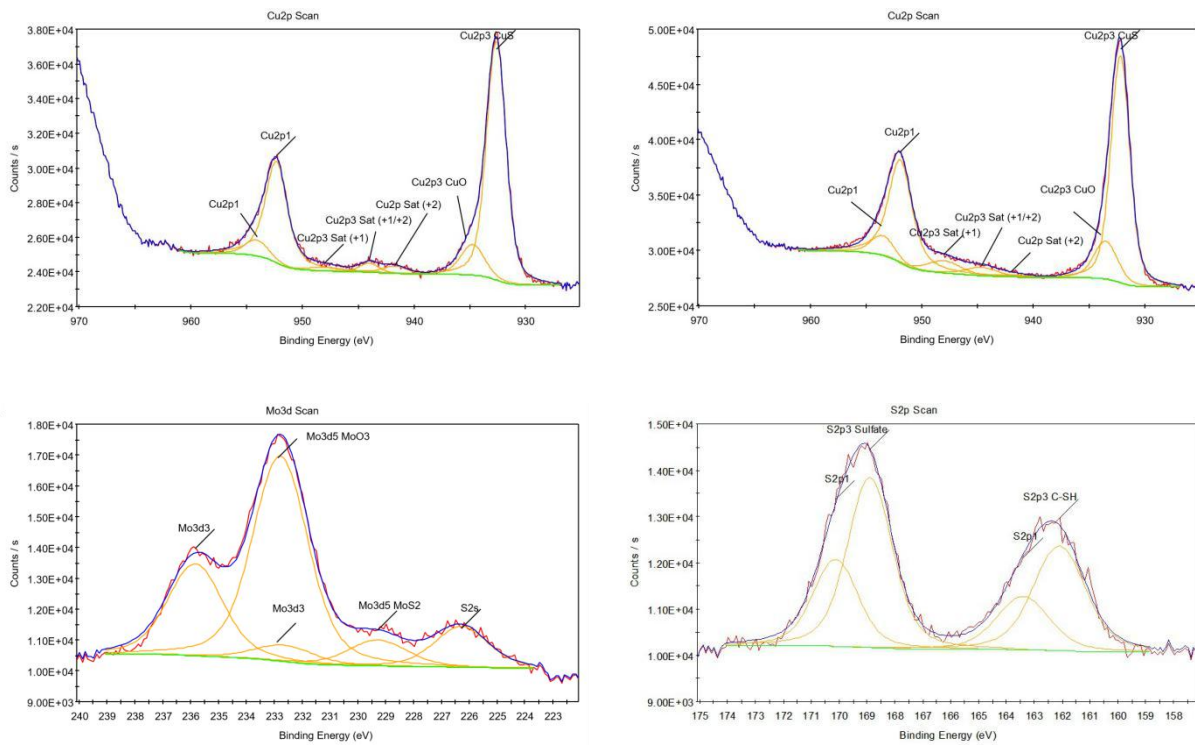


Figure 15. XPS spectra of CuMoS adsorbents

5.2.3 BET

To further evaluate the effect of adding Mo and increasing adsorbent quantities, we investigated surface area and pore properties of adsorbents. In Figure 16, the main trend showed that surface area and pore volume significantly decreased while the

amount of adsorbents increased. These trends of BET surface area and pore volume were typical of adsorbents which were synthesized by impregnation. This trend also showed in adsorbents with the addition of Mo. Based on this information, there was no direct relationship between the adsorption capacity of the adsorbent and BET surface area and pore structure.

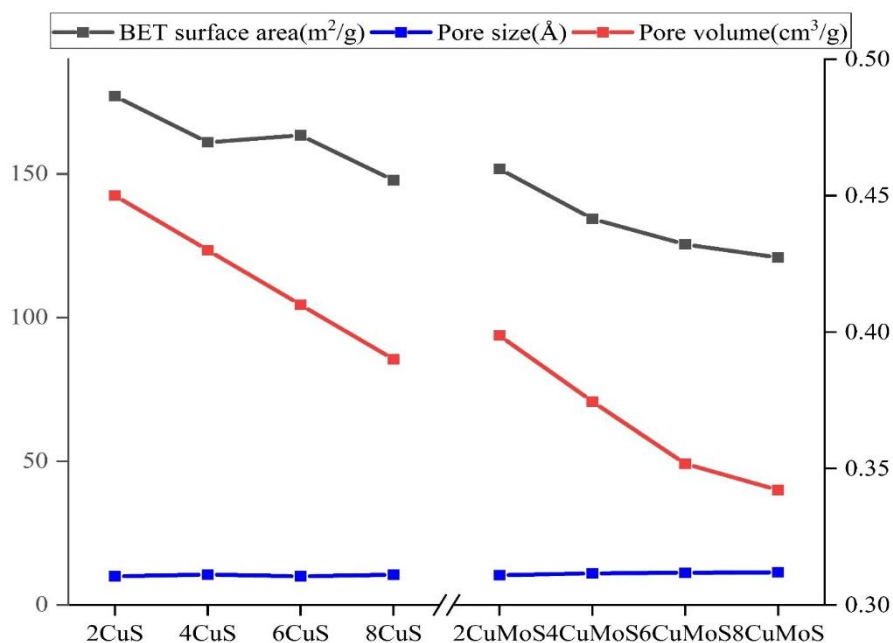


Figure 16. The surface properties of CuS and CuMoS adsorbents with different ratios of Cu

5.2.4 TEM

To study the morphology and structure characteristics of adsorbent, we used TEM and HRTEM to characterize 4%CuS and 4%CuMoS adsorbent(Figure 18). The layered structure was clearly observed in TEM images (Figure 18), showing that Cu₂S components were well dispersed on the surface of γ -Al₂O₃ carrier. The HRTEM image clearly showed a well-crystallized (102) lattice plane with a spacing of 0.24nm. After Mo was added, no significant changes were observed in HRTEM images. This was same with the XRD analysis. The change of Cu₂S content was so small that it was difficult to reflect these changes in HRTEM.

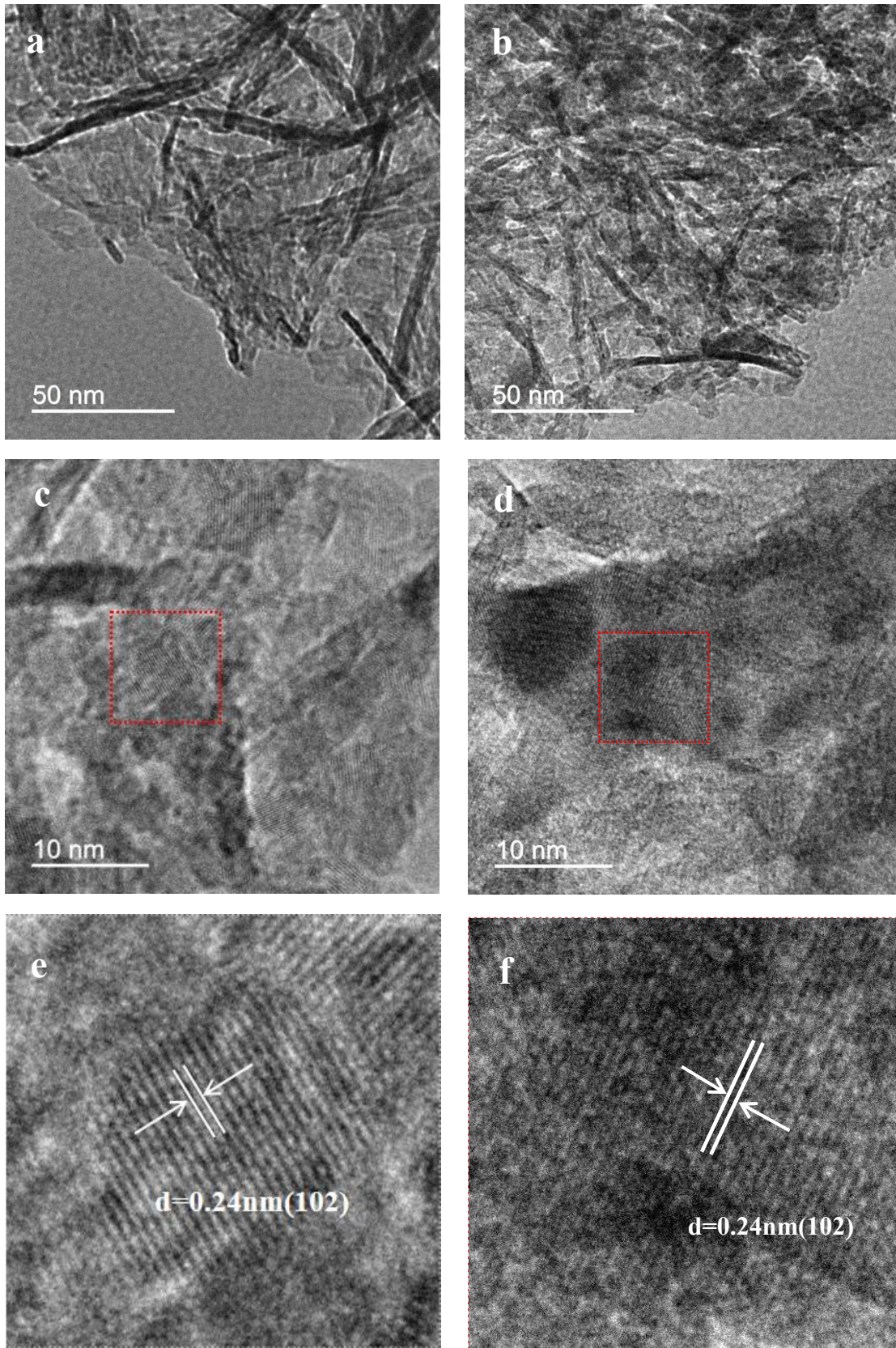


Figure 17. TEM images of a. (4%Cu2%S/ γ -Al₂O₃) b. (4%Cu8%Mo2%S/ γ -Al₂O₃) , HRTEM of c.and e. (4%Cu2%S/ γ -Al₂O₃) ,d. and f.(4%Cu8%Mo2%S/ γ -Al₂O₃).

5.3 Summary

In this chapter, CuS/ γ -Al₂O₃ and CuS-MoO₂/ γ -Al₂O₃ adsorbents with different Cu loading ratios were prepared by the same volume impregnation method. The removal of mercury from adsorbents was studied qualitatively and quantitatively by temperature-programmed surface reaction (TPSR). The relationship between adsorbent structure, composition and reactivity was studied by different characterization methods. The synergistic effect mechanism between CuS and Mo was revealed.

(1) TPSR analysis showed that when the Cu doping ratio was 4%, the effective mercury removal temperature of 4%Cu8%Mo2%S/ γ -Al₂O₃ adsorbent was the highest. The steady-state evaluation showed that, with the addition of MO, the effective adsorption temperature expanded from 100 °C to 150 °C, and the adsorption rate remained above 90%.

(2) XRD analysis showed that, with the addition of Mo, the strength of Cu²⁺ decreased. Combined with XPS analysis, Mo doping led to a higher proportion of Cu⁺ on the surface of the adsorbent, and part of Cu²⁺ was converted to Cu⁺, which had strong adsorption. After doped with MoO_x, the specific surface area of the catalyst decreased, which may be due to the Mo oxide immersed in the pores of the carrier and the blocked part of the carrier channel.

Chapter 6 Conclusions

In this paper, $\text{MnO}_2/\gamma\text{-Al}_2\text{O}_3$ and $\text{MnO}_2\text{-MoO}_3/\gamma\text{-Al}_2\text{O}_3$ catalysts with different Mn loading ratios and $\text{CuS}/\gamma\text{-Al}_2\text{O}_3$ and $\text{CuS-MoO}_3/\gamma\text{-Al}_2\text{O}_3$ adsorbents with different Cu loading ratios were prepared by the same volume impregnation method. The mercury removal effects of catalysts were studied from the qualitative and quantitative perspectives through the temperature-programmed surface reaction (TPSR). The influence of temperature on the mercury removal efficiency of the adsorbent was studied by steady-state analysis. The relationship between the structure, composition and reaction activity of the catalysts and the adsorbents by different characterization methods was studied. The main conclusions are as follows:

(1) In single metal Mn catalyst and MnMo bimetallic catalyst, when the Mn loading was 4%, $4\%\text{Mn}/\gamma\text{-Al}_2\text{O}_3$ and $1.25\%\text{Mo}4\%\text{Mn}/\gamma\text{-Al}_2\text{O}_3$ had the best catalytic effect. Dynamic analysis showed that $4\%\text{Mn}/\gamma\text{-Al}_2\text{O}_3$ had the best catalytic oxidation effect when the temperature was around 275°C . When Mo entered the catalyst as a dopant, $1.25\%\text{Mo}4\%\text{Mn}/\gamma\text{-Al}_2\text{O}_3$ catalyst can achieve the best catalytic oxidation efficiency (96%) at 202°C . XRD analysis showed that the pre-doping of Mo was conducive to the distribution of MnO_x on the carrier. This was consistent with the result of the representation of BET. Meanwhile, with the addition of Mo, the BET surface area was significantly increased. This indicated that with the addition of Mo, the activity of the catalyst was greatly enhanced. TEM can clearly observe that with the addition of molybdenum, the two layers of crystal surface overlapped, which provided more active sites for the catalyst. According to *in-situ* DRIFT analysis, there were more acidic sites on the surface of the Mo-Mn bimetallic catalyst, which was conducive to the adsorption of Hg^0 .

(2) In $\text{CuS}/\gamma\text{-Al}_2\text{O}_3$ adsorbents, all adsorbents had strong adsorption capacity and were above 90%. When the Cu doping ratio was 4%, the effective adsorption temperature window was the largest, and $4\%\text{Cu}2\%\text{S}/\gamma\text{-Al}_2\text{O}_3$ adsorbent can maintain the adsorption rate of more than 90% to Hg^0 in the range of $30\text{-}110^\circ\text{C}$. With the addition of MO, $4\%\text{Cu}8\%\text{Mo}2\%\text{S}/\gamma\text{-Al}_2\text{O}_3$ adsorbent's effective adsorption

temperature expanded from 100 °C to 150 °C, and the adsorption rate remained above 90%. XRD analysis showed that the strength of Cu^{2+} decreased with the addition of Mo. Combined with XPS analysis, Mo doping led to a higher proportion of Cu^+ on the surface of the adsorbent, and part of Cu^{2+} was converted into Cu^{1+} , which provided a stronger adsorption capacity of Hg^0 for the adsorbent. After doped with MoO_x , the specific surface area of the catalyst decreased, which may be because Mo oxide impregnated into the aperture of the carrier and blocked part of the carrier's channel.

(3) The addition of Mo led to a transition between Cu^{2+} and Cu^+ . The synergistic effect between MoO_x and Cu^{2+} promoted the adsorption capacity of the adsorbent to mercury. Meanwhile, the addition of Mo broadened the active temperature of the adsorbent and reduced the conditions of use.

(4) Combined with the exhaust removal of coal-fired power plants. In the WFDG system, the MoMn catalyst was used to catalyze the oxidation of over 90% Hg^0 , and the WFDG can directly remove most of the mercury vapor. The remaining small amount of mercury can be directly removed during the discharge process by means of a highly efficient CuMoS adsorbent. Such a combination could effectively reduce mercury emissions from coal-fired power plants.

References

1. Li, G., et al., *Mechanism identification of temperature influence on mercury adsorption capacity of different halides modified bio-chars*. Chemical Engineering Journal, 2017. **315**: p. 251-261.
2. Dinesh and P.T. Narasimhan, *Chlorine Nuclear Quadrupole Resonance Study of HgCl₂*. The Journal of Chemical Physics, 1966. **45**(6): p. 2170-2174.
3. Selin, H., *Global Environmental Law and Treaty-Making on Hazardous Substances: The Minamata Convention and Mercury Abatement*. Global Environmental Politics, 2014. **14**(1): p. 1-19.
4. Chen, Z., et al., *Anammox biofilm system under the stress of Hg(II): Nitrogen removal performance, microbial community dynamic and resistance genes expression*. Journal of Hazardous Materials, 2020. **395**.
5. Liu, Z., V. Sriram, and J.-Y. Lee, *Heterogeneous oxidation of elemental mercury vapor over RuO₂/rutile TiO₂ catalyst for mercury emissions control*. Applied Catalysis B: Environmental, 2017. **207**: p. 143-152.
6. Li, J.e.a., *Catalytic Oxidation of Elemental Mercury over the Modified Catalyst Mn/ α -Al₂O₃ at Lower Temperatures*. Environmental science & technology, 44(1), , 2010: p. pp.426–431.
7. Gao, Y., et al., *A critical review on the heterogeneous catalytic oxidation of elemental mercury in flue gases*. Environ Sci Technol, 2013. **47**(19): p. 10813-23.

8. Xu, H., et al., *MnOx/Graphene for the Catalytic Oxidation and Adsorption of Elemental Mercury*. Environ Sci Technol, 2015. **49**(11): p. 6823-30.
9. Zhao, H., et al., *Hg0-temperature-programmed surface reaction and its application on the investigation of metal oxides for Hg0 capture*. Fuel, 2016. **181**: p. 1089-1094.
10. Ghorishi, S.B., Lee, Chun W. Jozewicz, Wojciech S., *Effects of Fly Ash Transition Metal Content and Flue Gas HCl/SO2 Ratio on Mercury Speciation in Waste Combustion*. Environmental Engineering Science, 2005. **Vol. 22 Issue 2**: p. p221-231, 11p.
11. Mofarahi, M. and F. Gholipour, *Gas adsorption separation of CO2/CH4 system using zeolite 5A*. Microporous and Mesoporous Materials, 2014. **200**: p. 1-10.
12. Bei Liu, B.S., *Molecular Simulation Studies of Separation of CO2/N2, CO2/CH4, and CH4/N2 by ZIFs*. The Journal of Physical Chemistry, 2010. **114 (18)**: p. 8515-8522.
13. Na Chang, Z.-Y.G., and Xiu-Ping Yan, *Zeolitic Imidazolate Framework-8 Nanocrystal Coated Capillary for Molecular Sieving of Branched Alkanes from Linear Alkanes along with High-Resolution Chromatographic Separation of Linear Alkanes*. Journal of the American Chemical Society, 2010. **132 (39)**: p. 13645-13647.
14. R.W.Triebe, F.H.T., K.C.Khulbe, *Adsorption of methane, ethane and ethylene on molecular sieve zeolites*. Gas Separation & Purification, 1999.

- 10(1):** p. Pages 81-84.
15. Zhou, Z., et al., *Vanadium silicate (EVS)-supported silver nanoparticles: A novel catalytic sorbent for elemental mercury removal from flue gas*. Journal of Hazardous Materials, 2019. **375**: p. 1-8.
 16. Miller, B.G., *Formation and Control of Nitrogen Oxides*, in *Clean Coal Engineering Technology*. 2017. p. 507-538.
 17. Zhao, H., et al., *Graphene-like MoS₂ containing adsorbents for Hg⁰ capture at coal-fired power plants*. Applied Energy, 2017. **207**: p. 254-264.
 18. Ancora, M.P., et al., *Meeting Minamata: Cost-effective compliance options for atmospheric mercury control in Chinese coal-fired power plants*. Energy Policy, 2016. **88**: p. 485-494.
 19. Chen, Z., et al., *Industrial-scale investigations of anthracite combustion characteristics and NO emissions in a retrofitted 300 MWe down-fired utility boiler with swirl burners*. Applied Energy, 2017. **202**: p. 169-177.
 20. Guo, Y., et al., *Conversion of elemental mercury with a novel membrane catalytic system at low temperature*. Journal of Hazardous Materials, 2012. **213-214**: p. 62-70.
 21. He, W., et al., *Insight into the effect of facet-dependent surface and oxygen vacancies of CeO₂ for Hg removal: From theoretical and experimental studies*. Journal of Hazardous Materials, 2020. **397**.
 22. Liu, K.-H., et al., *Control of Hg⁰ and NO from coal-combustion flue gases*

- using MnO_x - CeO_x /mesoporous SiO_2 from waste rice husk. *Catalysis Today*, 2017. **297**: p. 104-112.
23. Pacyna, E.G., et al., *Global anthropogenic mercury emission inventory for 2000*. *Atmospheric Environment*, 2006. **40**(22): p. 4048-4063.
24. Zhang, L., et al., *Updated emission inventories for speciated atmospheric mercury from anthropogenic sources in China*. *Environ Sci Technol*, 2015. **49**(5): p. 3185-94.
25. Wei, Z.S., et al., *Elemental mercury oxidation from flue gas by microwave catalytic oxidation over $Mn/\gamma-Al_2O_3$* . *Journal of Industrial and Engineering Chemistry*, 2015. **24**: p. 315-321.
26. Xu, H., et al., *MnO_x /Graphene for the Catalytic Oxidation and Adsorption of Elemental Mercury*. *Environmental Science & Technology*, 2015. **49**(11): p. 6823-6830.
27. Miller, B.G., *Coal-Fired Emissions and Legislative Action*, in *Clean Coal Engineering Technology*. 2017. p. 311-417.
28. Zheng, Y., et al., *Review of technologies for mercury removal from flue gas from cement production processes*. *Progress in Energy and Combustion Science*, 2012. **38**(5): p. 599-629.
29. Lu, Y., et al., *Characteristics of Fly Ashes from Full-Scale Coal-Fired Power Plants and Their Relationship to Mercury Adsorption*. *Energy & Fuels*, 2007. **21**(4): p. 2112-2120.
30. Yang, J., et al., *Removal of elemental mercury from flue gas by recyclable*

- CuCl₂ modified magnetospheres catalyst from fly ash. Part 1. Catalyst characterization and performance evaluation.* Fuel, 2016. **164**: p. 419-428.
31. Roy, C., et al., *Collagenic waste and rubber based resin-cured biocomposite adsorbent for high-performance removal(s) of Hg(II), safranin, and brilliant cresyl blue: A cost-friendly waste management approach.* Journal of Hazardous Materials, 2019. **369**: p. 199-213.
 32. Ma, S., et al., *Research progress of pollutants removal from coal-fired flue gas using non-thermal plasma.* Renewable and Sustainable Energy Reviews, 2017. **67**: p. 791-810.
 33. Xu, H., et al., *Enhancing the catalytic oxidation of elemental mercury and suppressing sulfur-toxic adsorption sites from SO₂-containing gas in Mn-SnS₂.* Journal of Hazardous Materials, 2020. **392**.
 34. Tanabe, K.K. and S.M. Cohen, *Engineering a Metal-Organic Framework Catalyst by Using Postsynthetic Modification.* Angewandte Chemie International Edition, 2009. **48**(40): p. 7424-7427.
 35. Zhao, H., et al., *Hg⁰ Capture over CoMoS/ γ -Al₂O₃ with MoS₂ Nanosheets at Low Temperatures.* Environmental Science & Technology, 2016. **50**(2): p. 1056-1064.
 36. Wang, Z., et al., *Insights into the catalytic behavior of LaMnO₃ perovskite for Hg⁰ oxidation by HCl.* Journal of Hazardous Materials, 2020. **383**.
 37. Li, J.-r., et al., *Oxidation efficiency of elemental mercury in flue gas by SCR De-NO_x catalysts.* Journal of Fuel Chemistry and Technology, 2012. **40**(2):

- p. 241-246.
38. Yang, Y., et al., *Charge-distribution modulation of copper ferrite spinel-type catalysts for highly efficient Hg⁰ oxidation*. Journal of Hazardous Materials, 2021. **402**.
 39. Zhao, B., et al., *Catalytic oxidation of elemental mercury by Mn–Mo/CNT at low temperature*. Chemical Engineering Journal, 2016. **284**: p. 1233-1241.
 40. Gao, C., et al., *1T/2H MoS₂ nanoflowers decorated amorphous Mo–CoS_x skeleton: A ZIF-based composite electrocatalyst for the hydrogen evolution reaction*. Applied Surface Science, 2020. **515**.
 41. Hebbar Kannur, K., et al., *Synthesis and structural properties of Mo–S–N sputtered coatings*. Applied Surface Science, 2020. **527**.
 42. Zhao, H., et al., *MoO₃-adjusted δ -MnO₂ nanosheet for catalytic oxidation of Hg⁰ to Hg²⁺*. Applied Catalysis B: Environmental, 2020. **263**.
 43. Jia, S., et al., *TiO₂/CuS heterostructure nanowire array photoanodes toward water oxidation: The role of CuS*. Applied Surface Science, 2019. **463**: p. 829-837.
 44. Li, H., et al., *Oxidation and capture of elemental mercury over SiO₂–TiO₂–V₂O₅ catalysts in simulated low-rank coal combustion flue gas*. Chemical Engineering Journal, 2011. **169**(1-3): p. 186-193.
 45. Wang, H., et al., *Fullerene carbon dot catalytic amplification-aptamer assay platform for ultratrace As⁺³ utilizing SERS/RRS/Abs trifunctional Au*

- nanoprobes*. Journal of Hazardous Materials, 2021. **403**.
46. Kevin C, G., Christopher J, Zygarlicke, *Mercury transformations in coal combustion flue gas*. Fuel Processing Technology, 2000. **Volumes 65–66, June 2000**, : p. Pages 289-310
47. Xu, W., et al., *Mercury removal from coal combustion flue gas by modified fly ash*. Journal of Environmental Sciences, 2013. **25(2)**: p. 393-398.
48. Kokkinos, E., et al., *Study of elemental mercury removal from flue gases using Tetravalent manganese Feroxyhyte*. Chemical Engineering Journal, 2017. **315**: p. 152-158.
49. Zhao, Y., et al., *Elemental mercury removal from flue gas by CoFe₂O₄ catalyzed peroxymonosulfate*. J Hazard Mater, 2018. **341**: p. 228-237.
50. Ma, Y., et al., *Design of MnO₂/CeO₂-MnO₂ hierarchical binary oxides for elemental mercury removal from coal-fired flue gas*. J Hazard Mater, 2017. **333**: p. 186-193.
51. Liu, Y., H. Li, and J. Liu, *Theoretical prediction the removal of mercury from flue gas by MOFs*. Fuel, 2016. **184**: p. 474-480.
52. Zhao, Y., et al., *A novel catalytic oxidation process for removing elemental mercury by using diperiodatoargentate(III) in the catalysis of trace ruthenium(III)*. Journal of Hazardous Materials, 2020. **381**.
53. Ludwig, J., et al., *Ultrafast Hole Trapping and Relaxation Dynamics in p-Type CuS Nanodisks*. J Phys Chem Lett, 2015. **6(14)**: p. 2671-5.

54. Zhang, J., et al., *Visible light photocatalytic H₂-production activity of CuS/ZnS porous nanosheets based on photoinduced interfacial charge transfer*. Nano Lett, 2011. **11**(11): p. 4774-9.
55. Wang, P., et al., *Supernormal Conversion Anode Consisting of High-Density MoS₂ Bubbles Wrapped in Thin Carbon Network by Self-Sulfuration of Polyoxometalate Complex*. ACS Nano, 2017. **11**(7): p. 7390-7400.
56. Hou, Y., et al., *3D dual-confined sulfur encapsulated in porous carbon nanosheets and wrapped with graphene aerogels as a cathode for advanced lithium sulfur batteries*. Nanoscale, 2016. **8**(15): p. 8228-35.
57. Hsu C-J, Xiao Y-Z, Hsi H-C. Simultaneous aqueous Hg(II) adsorption and gaseous Hg₀ re-emission inhibition from SFGD wastewater by using Cu and S co-impregnated activated carbon. Chemosphere. 2021;263.